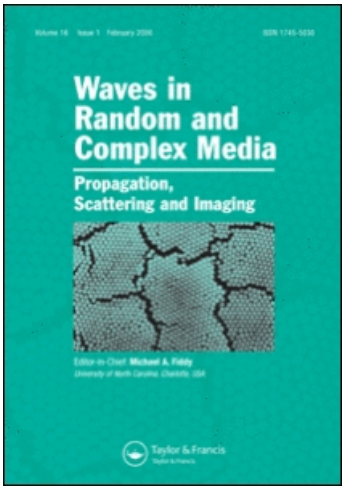

Waves in Random and Complex Media
Publication details, including instructions for authors and subscription information:
http://www.informaworld.com/smpp/title~content=t716100762

Numerical implementation of local unified models for backscattering from random rough sea surfaces

C. Bourlier [a]; N. Pinel [a]
[a] IREENA, Polytech Nantes-Université de Nantes, Nantes Cedex 3, France

To cite this Article Bourlier, C. and Pinel, N.(2009) 'Numerical implementation of local unified models for backscattering from random rough sea surfaces', Waves in Random and Complex Media, 19: 3, 455 — 479
To link to this Article: DOI: 10.1080/17455030902988931
URL: http://dx.doi.org/10.1080/17455030902988931

Waves in Random and Complex Media
Vol. 19, No. 3, August 2009, 455–479

Taylor & Francis
Taylor & Francis Group

Numerical implementation of local unified models for backscattering from random rough sea surfaces

C. Bourlier* and N. Pinel

IREENA, Polytech Nantes-Université de Nantes, La Chantrerie, Rue C. Pauc, BP 50609, 44306 Nantes Cedex 3, France

(*Received 19 December 2008; final version received 20 April 2009*)

In the context of electromagnetic wave backscattering from ocean-like surfaces, by using the lowest order of the SSA (SSA-1) model, Bourlier et al. proposed an original technique to reduce the number of numerical integrations to two for easier numerical implementation. To be consistent with microwave measurements, closed-form expressions of the Fourier coefficients with respect to the wind direction of the backscattering normalized radar cross-section (NRCS) are obtained. For Gaussian statistics, previous work is extended in this paper to kernels of unified models expanded up to second order, like full SSA and full LCA. Thus, with the help of Bessel functions and by analytical integrations over the azimuthal angles, the second-order backscattering (BNRCS) is expressed in terms of two-fold integrations and another independent integration instead of four-fold integrations, if no analytical integration is made. This approach allows us to obtain fast results (less than one second). Numerical results are then presented for different microwave frequencies and wind speeds.

1. Introduction

Since the 1960s, the derivation of the microwave backscattering normalized radar cross-section (BNRCS) from ocean surfaces is a topic of investigation which makes progress and remains a challenging task. The first developed model is the two-scale model (TSM) derived for acoustic waves by Kur'yanov [1] and for electromagnetic waves by Wright [2]. It is probably the most frequently employed approach, owing to its simple numerical implementation and to the fact that it gives satisfactory comparisons with measurements. Recently, this approach was improved [3–5] in order to minimize the effect of the scale-dividing parameter separating the small- and large-scale components of the roughness, and to increase the level of the cross-polarization. Moreover, another group of scattering models was proposed, namely the *local unified* models. The term *local* means that the multiple scattering phenomenon is neglected, and the term *unified* means that the model satisfies the high- and low-frequency limits given by the geometric optics approximation at the first order (GOA-1) and the small perturbation method at the first order (SPM-1), respectively. For more details, see the thorough review of Elfouhaily and Guérin [6]. One of the most popular is the SSA published by Voronovich [7,8]; more recently, models based on the same decomposition of the scattering matrix as SSA2 were published by Elfouhaily et al. [9,10].

For rough surfaces obeying a Gaussian process with 1-D or 2-D Gaussian spectra, the numerical implementation of such models for the computation of the NRCS can be done either

*Corresponding author. Email: christophe.bourlier@univ-nantes.fr

ISSN: 1745-5030 print / 1745-5049 online

DOI: 10.1080/17455030902988931
http://www.informaworld.com

from statistical formulas [11–15] or from a Monte Carlo procedure (see [16,17] and references therein). For a *multi*-scale sea 1-D surface, the numerical implementation of such models can be found in [18], whereas for a 2-D surface, quite small-size surfaces [19,20] are assumed for a Monte Carlo procedure, and additional assumptions are often necessary for the statistical formulas. For instance, in [21–24], only the small slope approximation at the first order (SSA-1) is considered, in [25], the partial second-order contribution in the NRCS is presented, and in [26], the phase perturbation technique (PPT) is applied to account for the small slope approximation at the second order (SSA-2) contribution in the NRCS. In [27], the PPT is also used to implement the local curvature approximation at the second order (LCA-2) developed by Elfouhaily et al. [9].

In general, the scattered field is expressed by an integral over the surface in which a kernel is involved, whose mathematical expression depends on the chosen asymptotic model. For instance, dealing with first-order asymptotic models, the local curvature approximation at the first order (LCA-1) kernel is equal to the one obtained from the Kirchhoff approximation at the first order (KA-1) combined with stationary phase approximation (SPA); the SSA-1 one has the same general form as the LCA-1 one, but the KA-1 polarization term is substituted for the SPM-1 one. The second-order term of the kernel is expressed in terms of an integral in the Fourier domain, and thus, it is more difficult to compute numerically. The BNRCS then requires four-fold numerical integrations.

From the SSA-1 model, Bourlier et al. [22,23] proposed a technique to reduce the number of numerical integrations to two, which strongly facilitates its numerical implementation. For the co-polarizations, this allows us to obtain closed-form expressions of the Fourier coefficients $\{\sigma_n\}$ of the backscattering NRCS σ in the form $\sigma = \sigma_0 + \sigma_1 \cos\phi + \sigma_2 \cos(2\phi)$, which is consistent with microwave measurements [28–34]. The angle ϕ is the observation azimuthal angle with respect to the wind direction, and the coefficients $\{\sigma_n\}$ depend on the observation elevation angle θ and on the wind speed. The isotropic backscattering term σ_0 mainly describes the wind speed, σ_1 the surface asymmetry along the up ($\phi = 0$) and down ($\phi = 180$ degrees) wind directions, and σ_2 the surface asymmetry along the up ($\phi = 0$) and cross ($\phi = 90$ degrees) wind directions.

The aim of this paper is to extend, for Gaussian statistics (corresponding to $\sigma_1 = 0$), the work of Bourlier and Berginc [22] to kernels expanded up to order two, like the SSA2 and the LCA2. The paper is organized as follows. In Section 2 some classical local unified scattering kernels are recalled, and in Section 3 the bistatic NRCS is derived, which is the main novelty of the paper. In Section 4 the BNRCS is derived, and Section 5 presents some comparisons between different kernels. In addition, an acceleration procedure is proposed to reduce the computing time. The last section gives concluding remarks.

2. Local unified scattering kernels

2.1. *Coordinates system and definition*

To describe the general problem in this paper, the same vectorial conventions as in [6] are used. A right-handed Cartesian coordinate system is defined by the triplet of normalized vectors $(\hat{\mathbf{x}}, \hat{\mathbf{y}}, \hat{\mathbf{z}})$ (the symbol $\hat{\mathbf{u}}$ stands for a unitary vector, $\hat{\mathbf{u}} = \mathbf{u}/\|\mathbf{u}\|$), where the z-axis is directed upward. Σ is the rough surface which separates the upper medium and the lower medium (respectively, the air and the sea in our case). The (sea) surface elevation is represented by $z = \eta(x, y) = \eta(\mathbf{r})$, where $\mathbf{r}$ is the horizontal component of the three-dimensional position vector $\mathbf{R} = (\mathbf{r}, z)$. The incident downward propagative electromagnetic plane wave is characterized by the wavevector $\mathbf{K}_0 = (\mathbf{k}_0, -q_0)$, and the up-going scattered wave by the wavevector $\mathbf{K} = (\mathbf{k}, q_k)$. The vectors $\mathbf{k}_0$ and $\mathbf{k}$ are the horizontal components of the incident and the scattered waves, whereas q_0 and q_k

are the vertical ones. We also define $\mathbf{Q}_H$ and Q_z related to the coordinates of the wavevectors $\mathbf{K}$ and $\mathbf{K}_0$ as $\mathbf{Q}_H = \mathbf{k} - \mathbf{k}_0$ and $Q_z = q_0 + q_k$, respectively.

The scattered field above and far away ($R \to \infty$) from the sea surface is assumed to be related to the incident wave through the relation

$$\mathbf{E}(\mathbf{R}) = -2j\pi \frac{e^{jkR}}{R} \bar{\mathbf{S}}(\mathbf{k}, \mathbf{k}_0) \cdot \hat{\mathbf{E}}_0, \tag{1}$$

where $\hat{\mathbf{E}}_0$ is the incident field, and $\bar{\mathbf{S}}(\mathbf{k}, \mathbf{k}_0)$ is the so-called scattering operator, which is a square matrix of size 2, expressed on the basis of plane waves defined with respect to the incident and the scattered waves. The symbol $\bar{}$ stands for a matrix. In what follows, the elements of the matrix $\bar{\mathbf{S}}$ will be denoted as $\{\mathcal{S}^{pq}\}$, with superscripts $p = \{V, H\}$ and $q = \{V, H\}$.

For a given polarization configuration pq, $\mathcal{S}^{pq}$ is written as

$$\mathcal{S}^{pq} = \frac{1}{Q_z} \int_{\mathbf{r}} \mathcal{N}^{pq}(\mathbf{k}, \mathbf{k}_0; \eta(\mathbf{r})) e^{-j[\mathbf{Q}_H \cdot \mathbf{r} + Q_z \eta(\mathbf{r})]} d\mathbf{r}, \tag{2}$$

where $\mathcal{N}^{pq}(\mathbf{k}, \mathbf{k}_0; \eta(\mathbf{r}))$ is a kernel which depends on the approach considered to establish the solution.

A general development of the kernel $\mathcal{N}^{pq}(\mathbf{k}, \mathbf{k}_0; \eta(\mathbf{r}))$ can lead to

$$\mathcal{N}^{pq}(\mathbf{k}, \mathbf{k}_0; \eta(\mathbf{r})) = \mathcal{N}_1^{pq}(\mathbf{k}, \mathbf{k}_0) + \mathcal{N}_2^{pq}(\mathbf{k}, \mathbf{k}_0; \eta(\mathbf{r})) + \mathcal{N}_3^{pq}(\mathbf{k}, \mathbf{k}_0; \eta(\mathbf{r})) + \cdots, \tag{3}$$

where the sub-kernels up to the third order are expressed from an inverse Fourier transform as

$$\begin{cases} \mathcal{N}_2^{pq}(\mathbf{k}, \mathbf{k}_0; \eta(\mathbf{r})) = \displaystyle\int_{\boldsymbol{\xi}} \hat{\mathcal{N}}_2^{pq}(\mathbf{k}, \mathbf{k}_0; \boldsymbol{\xi}) \hat{\eta}(\boldsymbol{\xi}) e^{j\boldsymbol{\xi} \cdot \mathbf{r}} d\boldsymbol{\xi} \\ \mathcal{N}_3^{pq}(\mathbf{k}, \mathbf{k}_0; \eta(\mathbf{r})) = \displaystyle\int_{\boldsymbol{\xi}} \int_{\boldsymbol{\xi}'} \hat{\mathcal{N}}_3^{pq}(\mathbf{k}, \mathbf{k}_0; \boldsymbol{\xi}, \boldsymbol{\xi}') \hat{\eta}(\boldsymbol{\xi}) \hat{\eta}(\boldsymbol{\xi}') e^{j(\boldsymbol{\xi} + \boldsymbol{\xi}') \cdot \mathbf{r}} d\boldsymbol{\xi} d\boldsymbol{\xi}', \end{cases} \tag{4}$$

where $\hat{\eta}(\boldsymbol{\xi})$ is the Fourier transform of the elevation $\eta(\mathbf{r})$. The notation $\hat{}$ means that the term is expressed in the spectral domain. As the order of the kernel increases, the number of integrations in the Fourier domain increases and thus the numerical complexity increases. In this paper, only kernels up to the second order will be studied.

Equations (2)–(4) show, up to second order, that the elements of the scattering matrix require the computation of two-fold 2-D integrals (one over the Fourier domain $\boldsymbol{\xi}$ and one over the spatial domain $\mathbf{r}$). When the range of length-scales in the surface is not too huge, these integrations can be done from an FFT algorithm. For a multi-scale ocean surface, the use of an FFT algorithm is rather time consuming. To overcome this issue, this paper presents a technique to reduce this computation to a two-fold integrand (one space variable and one frequency variable) by resorting to azimuthal harmonic expansion of the BNRCS.

2.2. *Some local unified kernels*

Asymptotic electromagnetic models predicting the scattered field from a rough surface can then rely on the expansion of the kernel $\mathcal{N}^{pq}(\mathbf{k}, \mathbf{k}_0; \eta(\mathbf{r}))$ in the scattering amplitude expression (2).

In particular, Elfouhaily et al. [9,10] and Voronovich [7] proposed different expressions for the kernel $\mathcal{N}^{pq}(\mathbf{k}, \mathbf{k}_0; \eta(\mathbf{r}))$, which are detailed in the following.

2.2.1. *LCA2 model*

The LCA2 sub-kernels established by Elfouhaily et al. are expressed as

$$\begin{cases} \mathcal{N}_1^{pq}(\mathbf{k}, \mathbf{k}_0) = \mathcal{K}_1^{pq}(\mathbf{k}, \mathbf{k}_0) \\ \hat{\mathcal{N}}_2^{pq}(\mathbf{k}, \mathbf{k}_0; \boldsymbol{\xi}) = -j\,Q_z \left[\mathcal{B}_1^{pq}\left(\frac{\mathbf{k}+\mathbf{k}_0+\boldsymbol{\xi}}{2}, \frac{\mathbf{k}+\mathbf{k}_0-\boldsymbol{\xi}}{2} \right) - \mathcal{K}_1^{pq}\left(\frac{\mathbf{k}+\mathbf{k}_0+\boldsymbol{\xi}}{2}, \frac{\mathbf{k}+\mathbf{k}_0-\boldsymbol{\xi}}{2} \right) \right]. \end{cases} \quad \text{LCA2} \tag{5}$$

The local curvature approximation up to the second order (LCA2) kernel satisfies the low- (SPM-1) and the high- (KA-1 combined with SPA) frequency limits to first order. $\mathcal{K}_1^{pq}(\mathbf{k}, \mathbf{k}_0)$ and $\mathcal{B}_1^{pq}(\mathbf{k}, \mathbf{k}_0)$ are the elements of the KA-1 and the SPM-1 polarization matrices, respectively. Their expressions can be found in [9,18].

To avoid integration over the variable $\boldsymbol{\xi}$ (so that $\hat{\mathcal{N}}_2^{pq}(\mathbf{k}, \mathbf{k}_0; \boldsymbol{\xi}) = 0$), Elfouhaily et al. [9] (for more details, see Subsection 5.1) proposed an alternative approach, namely the weighted curvature approximation at the first order (WCA-1), for which

$$\begin{cases} \mathcal{N}_1^{pq}(\mathbf{k}, \mathbf{k}_0) = \mathcal{B}_1^{pq}(\mathbf{k}, \mathbf{k}_0) - j\mathcal{N}_{\mathrm{LCA}-2}^{pq}(\mathbf{k}, \mathbf{k}_0; -Q_z \nabla\eta)\,/\,Q_z \\ \hat{\mathcal{N}}_2^{pq}(\mathbf{k}, \mathbf{k}_0; \boldsymbol{\xi}) = 0, \end{cases} \quad \text{WCA-1} \tag{6}$$

with

$$\nabla\eta = \frac{\partial\eta}{\partial x}\hat{\mathbf{x}} + \frac{\partial\eta}{\partial y}\hat{\mathbf{y}},$$

the slope vector of the surface.

Using a Monte Carlo process, the WCA-1 model is more convenient than the LCA-2 model, because its kernel requires the calculation of the slope vector $\nabla\eta$, instead of an integration over $\boldsymbol{\xi}$ for the LCA-2 sub-kernel. The second-order statistical moment of $\mathcal{S}^{pq}$ of the WCA-1 was derived rigorously by Bourlier [23] and was tested for a multi-scale Gaussian 1-D sea surface. It leads to the computation of three 2-D (1-D for a 1-D surface) integrals, because the statistical average over the surface slopes cannot be derived analytically, owing to the complexity of the kernel $\mathcal{N}_{\mathrm{LCA-2}}^{pq}$ over $\boldsymbol{\xi} = -Q_z\nabla\eta$. Thus, it is easier to implement the LCA2 model from statistical formulas than the WCA-1 model. The WCA-1 model was also tested by Guérin et al. [15] for a Gaussian 2-D surface with a Gaussian spectrum, for which the correlation between the slopes and the heights is neglected in the evaluation of the statistical formulas for the bistatic NRCS computation (thus, for this specific case, the numerical implementation of the WCA-1 model is easier than the LCA2 one). In this paper, this class of kernel will be not investigated.

2.2.2. *SSA2 model*

The small slope approximation up to the second order (SSA2) sub-kernels established by Voronovich [7] are expressed as

$$\begin{cases} \mathcal{N}_1^{pq}(\mathbf{k}, \mathbf{k}_0) & = \mathcal{B}_1^{pq}(\mathbf{k}, \mathbf{k}_0) \\ \hat{\mathcal{N}}_2^{pq}(\mathbf{k}, \mathbf{k}_0; \boldsymbol{\xi}) & = -\frac{j}{4}\big[\mathcal{B}_2^{pq}(\mathbf{k}, \mathbf{k}_0; \mathbf{k} - \boldsymbol{\xi}) \\ & \quad + \mathcal{B}_2^{pq}(\mathbf{k}, \mathbf{k}_0; \mathbf{k}_0 + \boldsymbol{\xi}) + 2Q_z\mathcal{B}_1^{pq}(\mathbf{k}, \mathbf{k}_0)\big]. \end{cases} \quad \text{SSA2} \tag{7}$$

Like the LCA2 and the WCA-1 models, the SSA2 model satisfies fundamental properties such as reciprocity, shift invariance, tilt variance and SPM-1 limit. However, the SSA2 does not satisfy the KA-1+SPA limit [35], but it satisfies the small perturbation method at the second order (SPM-2) limit. $\mathcal{B}_2^{pq}$ are the elements of the small perturbation method at the second order (SPM-2) polarization matrix and can be found in [7,18].

2.2.3. *The phase perturbation technique (PPT)*

From Equations (2), (3) and (4), $\mathcal{S}^{pq}(\mathbf{k}, \mathbf{k}_0)$ is expressed as

$$\mathcal{S}^{pq}(\mathbf{k}, \mathbf{k}_0) = \frac{1}{Q_z}\int_{\mathbf{r}} \big[\mathcal{N}_1^{pq}(\mathbf{k}, \mathbf{k}_0) + \mathcal{N}_2^{pq}(\mathbf{k}, \mathbf{k}_0; \eta(\mathbf{r}))\big] e^{-j[\mathbf{Q}_H \cdot \mathbf{r} + Q_z\eta(\mathbf{r})]} d\mathbf{r}, \tag{8}$$

where

$$\mathcal{N}_2^{pq}(\mathbf{k}, \mathbf{k}_0; \eta(\mathbf{r})) = \int_{\boldsymbol{\xi}} \hat{\mathcal{N}}_2^{pq}(\mathbf{k}, \mathbf{k}_0; \boldsymbol{\xi}) \hat{\eta}(\boldsymbol{\xi}) e^{j\boldsymbol{\xi}\cdot\mathbf{r}} d\boldsymbol{\xi}. \tag{9}$$

To take the second-order sub-kernel into account, the PPT states that (see [26,27], Equation (8))

$$\mathcal{S}^{pq}(\mathbf{k}, \mathbf{k}_0) \approx \frac{\mathcal{N}_1^{pq}(\mathbf{k}, \mathbf{k}_0)}{Q_z} \int_{\mathbf{r}} e^{-j\left[\mathbf{Q}_H \cdot \mathbf{r} + Q_z \eta_{PPT}^{pq}(\mathbf{r})\right]} d\mathbf{r}, \tag{10}$$

where

$$\eta_{PPT}^{pq}(\mathbf{r}) = \eta(\mathbf{r}) - \frac{\mathcal{N}_2^{pq}(\mathbf{k}, \mathbf{k}_0; \eta(\mathbf{r}))}{j\,Q_z\mathcal{N}_1^{pq}(\mathbf{k}, \mathbf{k}_0)} = \int_{\boldsymbol{\xi}} \left[1 - \frac{\hat{\mathcal{N}}_2^{pq}(\mathbf{k}, \mathbf{k}_0; \boldsymbol{\xi})}{j\,Q_z\mathcal{N}_1^{pq}(\mathbf{k}, \mathbf{k}_0)}\right] \hat{\eta}(\boldsymbol{\xi}) e^{j\boldsymbol{\xi}\cdot\mathbf{r}} d\boldsymbol{\xi}. \tag{11}$$

Thus, the scattering operator $\mathcal{S}^{pq}(\mathbf{k}, \mathbf{k}_0)$ is similar to a first-order operator, in which the elevation $\eta(\mathbf{r})$ is substituted for a filtered elevation $\eta_{PPT}^{pq}(\mathbf{r})$ which is polarization sensitive.

2.3. *Bistatic normalized radar cross-section (NRCS)*

The incoherent bistatic NRCS is proportional to the second-order centred statistical moment of the scattering operator $\mathcal{S}^{pq}(\mathbf{k}, \mathbf{k}_0)$

$$\sigma^{pq}(\mathbf{k}, \mathbf{k}_0) \propto \langle |\mathcal{S}^{pq}(\mathbf{k}, \mathbf{k}_0)|^2 \rangle - |\langle \mathcal{S}^{pq}(\mathbf{k}, \mathbf{k}_0) \rangle|^2. \tag{12}$$

From (8), assuming that the surface is stationary (i.e. spatially homogeneous), the second-order statistical moment of $\mathcal{S}^{pq}(\mathbf{k}, \mathbf{k}_0)$, $\langle|\mathcal{S}^{pq}(\mathbf{k}, \mathbf{k}_0)|^2\rangle$, becomes

$$\langle|\mathcal{S}^{pq}(\mathbf{k}, \mathbf{k}_0)|^2\rangle = \frac{A_0}{Q_z^2}\int_{\mathbf{r}} e^{-j\mathbf{Q}_H\cdot\mathbf{r}}\Big\{ \left|\mathcal{N}_1^{pq}\right|^2 \left\langle e^{jQ_z[\eta(\mathbf{r}_1)-\eta(\mathbf{r}_2)]}\right\rangle + \left\langle\left[\mathcal{N}_1^{pq}\left(\mathcal{N}_2^{pq}(\mathbf{r}_1)\right)^* + \left(\mathcal{N}_1^{pq}\right)^*\mathcal{N}_2^{pq}(\mathbf{r}_2)\right] e^{jQ_z[\eta(\mathbf{r}_1)-\eta(\mathbf{r}_2)]}\right\rangle\Big\} d\mathbf{r}. \tag{13}$$

The horizontal position vector, $\mathbf{r} = \mathbf{r}_2 - \mathbf{r}_1$, is defined as the difference between two horizontal position vectors $\mathbf{r}_1$ and $\mathbf{r}_2$. Since the surface is assumed to be stationary, the statistical averaging depends only on $\mathbf{r} = \mathbf{r}_2 - \mathbf{r}_1$. A_0 is the surface area. The symbol * stands for the complex conjugate. The term with respect to $\langle e^{jQ_z[\eta(\mathbf{r}_1)-\eta(\mathbf{r}_2)]}\mathcal{N}_2^{pq*}(\mathbf{r}_1)\mathcal{N}_2^{pq}(\mathbf{r}_2)\rangle$ is neglected because it represents a second-order contribution (i.e. in η^2), whereas the series expansion of the kernel is valid up to first order (i.e. in η).

For a Gaussian sea surface, the statistical averaging $\langle e^{jQ_z[\eta(\mathbf{r}_1)-\eta(\mathbf{r}_2)]}\rangle$ is given by

$$\chi(\mathbf{r}) = \left\langle e^{jQ_z[\eta(\mathbf{r}_1)-\eta(\mathbf{r}_2)]}\right\rangle = e^{-Q_z^2\left[\sigma_\eta^2 - W(\mathbf{r})\right]}, \tag{14}$$

where $W(\mathbf{r}) = \langle\eta(\mathbf{r}_1)\eta(\mathbf{r}_2)\rangle$ is the surface height autocorrelation function (which is an even function, $W(-\mathbf{r}) = W(\mathbf{r})$), and $\sigma_\eta^2 = W(\mathbf{0})$ its height variance.

In Equation (13), the derivation of the second statistical averaging is not straightforward; that is why it is reported in Appendix 1. Thus, from Equations (50) and (52), we have

$$\langle|\mathcal{S}^{pq}(\mathbf{k}, \mathbf{k}_0)|^2\rangle = \frac{A_0}{Q_z^2}\int_{\mathbf{r}} e^{-j\mathbf{Q}_H\cdot\mathbf{r}}\chi(\mathbf{r})\left[\left|\mathcal{N}_1^{pq}\right|^2 + \mathcal{N}_1^{pq}\left(\chi_1^{pq}(-\mathbf{r})\right)^* + \left(\mathcal{N}_1^{pq}\right)^*\chi_1^{pq}(\mathbf{r})\right] d\mathbf{r}, \tag{15}$$

with

$$\chi_1^{pq}(\mathbf{r}) = jQ_z\left[W_m^{pq}(\mathbf{r}) - W_m^{pq}(\mathbf{0})\right], \tag{16}$$

and

$$W_m^{pq}(\mathbf{r}) = \int_{\boldsymbol{\xi}} \hat{\mathcal{N}}_2^{pq}(\boldsymbol{\xi})\hat{W}(\boldsymbol{\xi})e^{j\boldsymbol{\xi}\cdot\mathbf{r}}d\boldsymbol{\xi}. \tag{17}$$

$\hat{W}_2(\boldsymbol{\xi})$ is the sea height spectrum, and $W_m^{pq} \in \mathbb{C}$ is the modified height correlation function. In addition, since

$$|\langle\mathcal{S}^{pq}(\mathbf{k}, \mathbf{k}_0)\rangle|^2 = \lim_{\mathbf{r}\to\infty}\langle|\mathcal{S}^{pq}(\mathbf{k}, \mathbf{k}_0)|^2\rangle, \tag{18}$$

the bistatic NRCS $\sigma^{pq}(\mathbf{k}, \mathbf{k}_0)$, proportional to Equation (12), is expressed as

$$\sigma^{pq}(\mathbf{k}, \mathbf{k}_0) = A\int_{\mathbf{r}} e^{-j\mathbf{Q}_H\cdot\mathbf{r}}\Big(\chi(\mathbf{r})\left[\left|\mathcal{N}_1^{pq}\right|^2 + \mathcal{N}_1^{pq}\left(\chi_1^{pq}(-\mathbf{r})\right)^* + \left(\mathcal{N}_1^{pq}\right)^*\chi_1^{pq}(\mathbf{r})\right] - e^{-Q_z^2\sigma_\eta^2}\left\{\left|\mathcal{N}_1^{pq}\right|^2 + 2\mathrm{Re}\left[\left(\mathcal{N}_1^{pq}\right)^*\chi_1^{pq}(\infty)\right]\right\}\Big) d\mathbf{r}, \tag{19}$$

where

$$\chi_1^{pq}(\infty) = -jQ_z W_m^{pq}(\mathbf{0}), \quad \text{and} \quad A = \frac{1}{\pi(q_0+q_k)^2}. \tag{20}$$

It can be noted that $W(\infty) = W_m(\infty) = 0$.

Equation (6.8) of [7] is found, in which the minus sign inside $F_{\alpha\alpha_0}^{NN_0}(\mathbf{k}, \mathbf{k}_0; \mathbf{r})$ in front of $\mathbf{r}$ is missing in the last line. This typographical error was corrected in the paper of Berginc (see Equation (30) of [13]). McDaniel [25] has the same form as Equation (19).

In the paper of Mouche et al. (see Equation (24) of [27]), the term $\mathcal{N}_1^{pq}(\chi_1^{pq}(-\mathbf{r}))^* + (\mathcal{N}_1^{pq})^*\chi_1^{pq}(\mathbf{r})$ in Equation (19) is replaced by $2\mathrm{Re}(\mathcal{N}_1^{pq}\chi_1^{pq}(\mathbf{r}))$, and the coherent term is omitted. The former is true if $(\chi_1^{pq}(-\mathbf{r}))^* = \chi_1^{pq}(\mathbf{r})$ and if $\chi_1^{pq}(\mathbf{r}) = (\chi_1^{pq}(\mathbf{r}))^*$, which implies that $W_m^{pq}(\mathbf{r})$ must satisfy the same properties (in Equation (16), the term jQ_z does not appear). These equalities are satisfied if $\hat{\mathcal{N}}_2^{pq}(\boldsymbol{\xi})$ has some particular properties. It is important to note that $\hat{W}(\boldsymbol{\xi}) \in \mathbb{R}$ and that $\hat{W}(-\boldsymbol{\xi}) = \hat{W}(\boldsymbol{\xi})$.

From Equation (19), the integrand $\mathcal{I}^{pq}(\mathbf{k}, \mathbf{k}_0; \mathbf{r}) = e^{-j\mathbf{Q}_H\cdot\mathbf{r}}\mathcal{I}_1^{pq}(\mathbf{k}, \mathbf{k}_0; \mathbf{r})$ satisfies $(\mathcal{I}_1^{pq}(\mathbf{k}, \mathbf{k}_0; -\mathbf{r}))^* = \mathcal{I}_1^{pq}(\mathbf{k}, \mathbf{k}_0; \mathbf{r})$, which ensures that $\sigma^{pq}(\mathbf{k}, \mathbf{k}_0)$ is real.

With the PPT and from (14), the bistatic NRCS σ^{pq} can be written as

$$\sigma^{pq}(\mathbf{k}, \mathbf{k}_0) \approx A\left|\mathcal{N}_1^{pq}(\mathbf{k}, \mathbf{k}_0)\right|^2 e^{-Q_z^2\mathrm{Re}\left[W_{PPT}^{pq}(\mathbf{0})\right]}\int_{\mathbf{r}} e^{-j\mathbf{Q}_H\cdot\mathbf{r}}\left[e^{Q_z^2\mathrm{Re}\left[W_{2,PPT}^{pq}(\mathbf{r})\right]} - 1\right]d\mathbf{r}, \tag{21}$$

with

$$W_{PPT}^{pq}(\mathbf{r}) = \int_{\boldsymbol{\xi}}\left|1 - \frac{\hat{\mathcal{N}}_2^{pq}(\mathbf{k}, \mathbf{k}_0; \boldsymbol{\xi})}{jQ_z\mathcal{N}_1^{pq}(\mathbf{k}, \mathbf{k}_0)}\right|^2 \hat{W}(\boldsymbol{\xi})e^{j\boldsymbol{\xi}\cdot\mathbf{r}}d\boldsymbol{\xi}. \tag{22}$$

It is important to note that W_{PPT}^{pq} is real if the kernel $\hat{\mathcal{N}}_2^{pq}(\mathbf{k}, \mathbf{k}_0; \boldsymbol{\xi})$ is even ($\hat{\mathcal{N}}_2^{pq}(\mathbf{k}, \mathbf{k}_0; -\boldsymbol{\xi}) = \hat{\mathcal{N}}_2^{pq}(\mathbf{k}, \mathbf{k}_0; \boldsymbol{\xi})$) since $\hat{W}(-\boldsymbol{\xi}) = \hat{W}(\boldsymbol{\xi}) \in \mathbb{R}$.

3. BNRCS

The calculation of the bistatic NRCS requires the computation of two 2-D integrals over $\mathbf{r}$ and $\boldsymbol{\xi}$. For a multi-scale sea surface, gravity and capillarity waves can contribute simultaneously to the scattering process, which implies that the height spectrum must account for both the low- and high-frequency regimes, making the four numerical integrations difficult to compute. In this section, for any kernel and in the backscattering direction ($\mathbf{k} = -\mathbf{k}_0 \Rightarrow A = \frac{1}{4\pi K^2\cos^2\theta}$), we propose to reduce the number of integrations to two by using the azimuthal properties of the statistical moments.

In the literature, from microwave (C and K_u bands for instance) experimental data [28–34], the backscattering NRCS (BNRCS) can be expressed for $pq = \{VV, HH\}$ co-polarizations in the form

$$\sigma^{pq}(-\mathbf{k}_0, \mathbf{k}_0) \equiv \sigma^{pq}(\theta, \phi; u) = \sigma_0^{pq}(\theta; u) + \sigma_1^{pq}(\theta; u)\cos\phi + \sigma_2^{pq}(\theta; u)\cos(2\phi), \tag{23}$$

where ϕ is the observation azimuthal angle with respect to the wind direction, θ the observation elevation angle, and u the wind speed. The isotropic backscattering term σ_0^{pq} mainly describes the wind speed, σ_1^{pq} the surface asymmetry along the up ($\phi = 0$) and down ($\phi = 180$ degrees)

wind directions, and σ_2^{pq} the surface asymmetry along the up ($\phi = 0$) and cross ($\phi = 90$ degrees) wind directions. For Gaussian statistics, $\sigma_1^{pq} = 0$.

To isolate the coefficients $\{\sigma_n^{pq}(\theta; u)\}$, each side of Equation (23) is multiplied by $\cos(n\phi)$ (with $n = \{0, 1, 2\}$) and integrated over $\phi \in [0; 2\pi[$, leading to

$$\sigma_n^{pq}(\theta; u) = \frac{1}{e_n \pi} \int_0^{2\pi} \sigma^{pq}(-\mathbf{k}_0, \mathbf{k}_0) \cos(n\phi) d\phi, \tag{24}$$

with $e_n = 2$ if $n = 0$; 1 otherwise. This decomposition can be interpreted as a Fourier series decomposition of the BNRCS σ^{pq}.

3.1. *Case where $\hat{\mathcal{N}}_2^{pq}(\boldsymbol{\xi}) = 0$*

For $\hat{\mathcal{N}}_2^{pq}(\boldsymbol{\xi}) = 0$ and using a polar coordinate system, $\mathbf{r} = (r\cos\phi_r, r\sin\phi_r)$ and $\mathbf{k}_0 = (k\sin\theta\cos\phi, k\sin\theta\sin\phi)$, Equation (19) becomes (with $Q_z^2 = 4q_0^2$)

$$\begin{aligned}\sigma_{11}^{pq}(-\mathbf{k}_0, \mathbf{k}_0) = A \left|\mathcal{N}_1^{pq}(-\mathbf{k}_0, \mathbf{k}_0)\right|^2 e^{-Q_z^2\sigma_\eta^2} \int_0^\infty \int_0^{2\pi} e^{jk_B r\cos(\phi-\phi_r)} \\ \times \left\{e^{Q_z^2[W_0(r)-\cos(2\phi_r)W_2(r)]} - 1\right\} r d\phi_r dr,\end{aligned} \tag{25}$$

where

$$\begin{cases} W_2(r, \phi_r) = W_0(r) - \cos(2\phi_r) W_2(r) \\ W_0(r) = \displaystyle\int_0^\infty \hat{W}_0(\xi) J_0(r\xi) d\xi \\ W_2(r) = \displaystyle\int_0^\infty \hat{W}_2(\xi) J_2(r\xi) d\xi, \end{cases} \tag{26}$$

and $\hat{W}_2(\xi) = \hat{W}_0(\xi)\hat{\Delta}(\xi)$, $k_B = 2K\sin\theta$ is the Bragg wavenumber. In (25), the subscript 11 means that the BNRCS results from the autocorrelation of the first-order scattered field. Similarly, in what follows, the subscript 12 means that the NRCS results from the correlation between the first-order and the second-order scattered fields.

$W_0(r)$ is the isotropic part of the height correlation function W, whereas $W_2(r)$ is its anisotropic part (J_n being the n-th order Bessel function of the first kind). They are computed from the isotropic part $\hat{W}_0(\xi)$ of the sea spectrum and its spreading function $\hat{\Delta}(\xi)$. It is assumed that $\hat{W}(\xi, \phi_\xi) = \hat{W}_0(\xi)[1 + \hat{\Delta}(\xi)\cos(2\phi_\xi)]/(2\pi)$, which is consistent with the sea spectrum model of Elfouhaily et al. [36].

Appendix 2 computes the integration over ϕ_r. From (56), the integration over ϕ_r of Equation (25) leads to

$$\begin{aligned}\sigma_{11}^{pq}(-\mathbf{k}_0, \mathbf{k}_0) = 2\pi A \left|\mathcal{N}_1^{pq}(-\mathbf{k}_0, \mathbf{k}_0)\right|^2 e^{-Q_z^2\sigma_\eta^2} \\ \times \int_0^\infty \left\{e^{Q_z^2 W_0(r)} \Psi_0\left(k_B r, Q_z^2 W_2(r), \phi\right) - J_0(k_B r)\right\} r dr,\end{aligned} \tag{27}$$

where $\Psi_0(k_B r, 0, \phi) = J_0(k_B r)$. Thus, from Equations (56) and (23), we have

$$\begin{cases} \sigma_{11,0}^{pq}(\theta;u) = 2\pi A \left|\mathcal{N}_1^{pq}(\theta)\right|^2 e^{-Q_z^2\sigma_\eta^2} \displaystyle\int_0^\infty J_0(k_B r)\left[e^{Q_z^2 W_0(r)} I_0\left(Q_z^2 W_2(r)\right) - 1\right] r dr \\ \sigma_{11,1}^{pq}(\theta;u) = 0 \\ \sigma_{11,2}^{pq}(\theta;u) = 4\pi A \left|\mathcal{N}_1^{pq}(\theta)\right|^2 e^{-Q_z^2\sigma_\eta^2} \displaystyle\int_0^\infty e^{Q_z^2 W_0(r)} J_2(k_B r) I_1\left(Q_z^2 W_2(r)\right) r dr, \end{cases} \tag{28}$$

where I_m denotes the Bessel function of the second kind and of order m. For an isotropic surface, $W_2(r)$ vanishes and $\sigma_{11,2}^{pq}(\theta;u) = 0$ because $I_1(0) = 0$. As expected, $\sigma_{11,1}^{pq}(\theta;u) = 0$ because Gaussian statistics are assumed. To be consistent with expansion (23), the sum (56) must be truncated to order 1 ($m < 2$), which means that the terms $\{J_{2m}(k_B r) I_m\left(Q_z^2 W_2(r)\right)\}$ can be neglected for $m > 1$. In addition, the decomposition (56) shows that the terms $\sin(n\phi)$ cannot appear.

Eventually, from Equation (28), the computation of the backscattering NRCS requires one numerical integration over the radial distance r, and one numerical integration over the wavenumber ξ for the computation of the surface height correlation functions $\{W_0(r), W_2(r)\}$ given by Equation (26).

3.2. *Case where $\hat{\mathcal{N}}_2^{pq}(\boldsymbol{\xi}) \neq 0$*

For $\hat{\mathcal{N}}_2^{pq}(\boldsymbol{\xi}) \neq 0$, the BNRCS σ_{12}^{pq} related to $\hat{\mathcal{N}}_2^{pq}(\boldsymbol{\xi})$ can be written from Equation (19) as

$$\begin{aligned} \sigma_{12}^{pq}(-\mathbf{k}_0, \mathbf{k}_0) = A \int_0^\infty \int_0^{2\pi} & e^{jk_B r\cos(\phi-\phi_r)} \\ & \times \left[\chi(r,\phi_r) G^{pq}(r,\phi_r) - \chi(\infty,\phi_r) G^{pq}(\infty,\phi_r)\right] r d\phi_r dr, \end{aligned} \tag{29}$$

with

$$\begin{cases} \chi(r,\phi_r) = e^{-Q_z^2\left[\sigma_\eta^2 - W_0(r) + \cos(2\phi_r) W_2(r)\right]} \\ G^{pq}(r,\phi_r) = \displaystyle\int_0^\infty \int_0^{2\pi} \hat{W}(\xi,\phi_\xi) \hat{G}^{pq}(\xi,\phi_\xi)\left[e^{j\xi r\cos(\phi_\xi-\phi_r)} - 1\right] d\phi_\xi d\xi \\ G^{pq}(\infty,\phi_r) = -\displaystyle\int_0^\infty \int_0^{2\pi} \hat{W}(\xi,\phi_\xi) \hat{G}^{pq}(\xi,\phi_\xi) d\phi_\xi d\xi, \end{cases} \tag{30}$$

$$\begin{cases} \hat{G}^{pq}(\xi,\phi_\xi) = -2Q_z \mathrm{Im}\left[\left(\mathcal{N}_1^{pq}\right)^* \hat{\mathcal{N}}_2^{pq}(\xi,\phi_\xi)\right] \\ \hat{G}^{pq}(\xi,\phi_\xi) = -2Q_z \mathrm{Im}\left[\left(\mathcal{N}_1^{pq}\right)^* \hat{\mathcal{N}}_2^{pq}(\xi,\phi_\xi)\right] + \left|\hat{\mathcal{N}}_2^{pq}(\xi,\phi_\xi)\right|^2 \quad \text{PPT}, \end{cases} \tag{31}$$

and $\hat{W}(\boldsymbol{\xi}) d\boldsymbol{\xi} = \hat{W}(\xi,\phi_\xi) d\phi_\xi d\xi$ (the term ξ is absorbed in the sea spectrum $\hat{W}(\xi,\phi_\xi)$). The symbol Im stands for the imaginary part. It is important to note that, under the PPT, the term $\hat{G}^{pq}$

is derived from Equations (21) and (22) by using the series expansion $e^x \approx 1 + x$. By comparison, the scattered field (10) derived under the PPT uses the reverse way, that is to say the approximation $1 + x \approx e^x$.

In the backscattering direction, we show in Appendices 3 and 4 that the sub-kernel $\hat{\mathcal{N}}_2^{pq}(-\mathbf{k}_0, \mathbf{k}_0; \boldsymbol{\xi})$ of SSA-2 is a periodic function with respect to $\phi_\xi - \phi$, whereas that of LCA-2 is a periodic function with respect to ϕ_ξ. Thus, the function $\hat{G}^{pq}(\xi, \phi_\xi)$ can be written as a Fourier series in the form

$$\hat{G}^{pq}(\xi, \phi_\xi) = \sum_{s=-\infty}^{+\infty} \hat{G}_s^{pq}(\xi) e^{js(\phi_\xi - \nu\phi)}, \tag{32}$$

where

$$\hat{G}_s^{pq}(\xi) = \frac{1}{2\pi} \int_0^{2\pi} \hat{G}^{pq}(\xi, \phi_\xi - \nu\phi) e^{-js(\phi_\xi - \nu\phi)} d(\phi_\xi - \nu\phi), \tag{33}$$

and $\nu = 1$ for the SSA-2 sub-kernel, whereas $\nu = 0$ for the LCA-2 one.

We show in Appendix 5 that

$$\begin{aligned}\sigma_{12,n}^{pq}(\theta; u) = 2A\pi e^{-Q_z^2\sigma_\eta^2} \int_0^\infty \int_0^\infty r d\xi dr \sum_{s=-\infty}^{+\infty} \hat{G}_s^{pq}(\xi) \\ \times \Big(\hat{W}_0(\xi) \left\{ e^{Q_z^2 W_0(r)} \left[\Omega_{n,s}^{(0)}(a, b, c) - \Omega_{n,s}^{(0)}(a, b, 0) \right] + \Omega_{n,s}^{(0)}(a, 0, 0) \right\} \\ + \hat{W}_2(\xi) \left\{ e^{Q_z^2 W_0(r)} \left[\Omega_{n,s}^{(2)}(a, b, c) - \Omega_{n,s}^{(2)}(a, b, 0) \right] + \Omega_{n,s}^{(2)}(a, 0, 0) \right\} \Big),\end{aligned} \tag{34}$$

with

$$\begin{aligned}\Omega_{n,s}^{(0)}(a, b, c) = \tfrac{(-1)^s}{2} J_s(c) \sum_{\gamma=\pm1} J_{n\gamma+s\nu}(a) I_{\frac{m_0}{2}}(b) \\ \text{with } m_0 = n\gamma - s + s\nu \text{ even; 0 otherwise,}\end{aligned} \tag{35}$$

$$\begin{aligned}\Omega_{n,s}^{(2)}(a, b, c) = \tfrac{(-1)^s}{4} \sum_{\gamma_1=\pm1} \sum_{\gamma_2=\pm1} J_{s+2\gamma_2}(c) J_{n\gamma_1+s\nu}(a) I_{\frac{m_0}{2}}(b) \\ \text{with } m_0 = n\gamma_1 - s - 2\gamma_2 + s\nu \text{ even; 0 otherwise,}\end{aligned} \tag{36}$$

and $a = k_B r$, $b = Q_z^2 W_2(r)$, $c = \xi r$. It can be noted that

$$\begin{cases} \Omega_{n,s}^{(0)}(a, b, 0) = \frac{\delta_{s,0}}{2} \sum_{\gamma=\pm1} J_{n\gamma}(a) I_{\frac{n\gamma}{2}}(b) \\ \Omega_{n,s}^{(2)}(a, b, 0) = \frac{\delta_{s,-2}+\delta_{s,+2}}{4} \sum_{\gamma=\pm1} J_{n\gamma+s\nu}(a) I_{\frac{n\gamma+s\nu}{2}}(b), \end{cases} \tag{37}$$

$$\begin{cases} \Omega_{n,s}^{(0)}(a,0,0) = J_0(a)\delta_{s,0}\delta_{n,0} \\ \Omega_{n,s}^{(2)}(a,0,0) = J_0(a)\delta_{s,\pm 2}\delta_{n,\pm 2\nu}, \end{cases} \tag{38}$$

and

$$\begin{cases} \Omega_{n,s}^{(0)}(0,0,0) = \delta_{s,0}\delta_{n,0} \\ \Omega_{n,s}^{(2)}(0,0,0) = \delta_{s,\pm 2}\delta_{n,\pm 2\nu}. \end{cases} \tag{39}$$

3.2.1. *LCA2 case*

We show in Appendix 4 that the LCA-2 sub-kernel $\hat{\mathcal{N}}_2^{pq}(\boldsymbol{\xi})$ is an even function with respect to ξ, which means that it is independent of the functions $\cos\phi_\xi$ and $\sin\phi_\xi$ ($\nu = 0$). Thus, the Fourier coefficients $\{\hat{G}_s(\xi)\}$ vanish for $s \neq 0$, implying that the sum over s is reduced to $s = 0$. Moreover, Equations (35) and (36) are simplified at $s = 0$ as

$$\begin{cases} \Omega_{n,0}^{(0)}(a,b,c) = J_0(c)J_n(a)I_{\frac{n}{2}}(b) & n \text{ even; 0 otherwise} \\ \Omega_{n,0}^{(2)}(a,b,c) = \frac{1}{2}J_2(c)J_n(a)\left[I_{\frac{n-2}{2}}(b) + I_{\frac{n+2}{2}}(b)\right] & n \text{ even; 0 otherwise.} \end{cases} \tag{40}$$

As expected, $\Omega_{1,0}^{(0)}$ and $\Omega_{1,0}^{(2)}$ ($n = 1$) vanish, which means that the BNRCS is independent of $\cos\phi$.

Equation (34) becomes

$$\begin{aligned} \sigma_{12,n}^{pq}(\theta;u) = 2A\pi e^{-Q_z^2\sigma_\eta^2}\int_0^\infty\int_0^\infty r\,d\xi\,dr\,\hat{G}_0^{pq}(\xi) \\ \times\left(\hat{W}_0(\xi)J_n(a)\left\{e^{Q_z^2W_0(r)}I_{\frac{n}{2}}(b)\left[J_0(c)-1\right]-\delta_{n,0}\right\}\right. \\ \left.+\frac{1}{2}\hat{W}_2(\xi)e^{Q_z^2W_0(r)}J_n(a)J_2(c)\left[I_{\frac{n-2}{2}}(b)+I_{\frac{n+2}{2}}(b)\right]\right),\ n \text{ even.} \end{aligned} \tag{41}$$

3.2.2. *SSA2 case*

We show in Appendix 3 that the SSA-2 sub-kernel $\hat{\mathcal{N}}_2^{pq}(\boldsymbol{\xi})$ is independent of the function $\sin(\phi_\xi - \nu\phi)$ ($\nu = 1$). In addition, since $\hat{G}^{pq}(\xi,\phi_\xi)$ is real, $\hat{G}^{pq}(\xi,\phi_\xi)$ is in consequence even, and the Fourier coefficients $\{\hat{G}_s(\xi)\}$ are real and satisfy $\hat{G}_{-s}(\xi) = \hat{G}_s(\xi) \in \mathbb{R}$. From this property, the sum over s can be reduced to $s \geq 1$, and we have with $\nu = 1$

$$\begin{aligned} \sum_{s=-\infty}^{+\infty}\hat{G}_s^{pq}(\xi)\Omega_{n,s}^{(0)}(a,b,c) = \hat{G}_0^{pq}(\xi)\Omega_{n,0}^{(0)}(a,b,c) \\ +\sum_{s=1}^{+\infty}\hat{G}_s^{pq}(\xi)J_s(c)I_{\frac{n}{2}}(b)\left[(-1)^sJ_{n+s}(a)+J_{n-s}(a)\right] \quad n \text{ even; 0 otherwise,} \end{aligned} \tag{42}$$

and

$$\begin{aligned} \sum_{s=-\infty}^{+\infty}\hat{G}_s^{pq}(\xi)\Omega_{n,s}^{(2)}(a,b,c) = \hat{G}_0^{pq}(\xi)\Omega_{n,0}^{(2)}(a,b,c) + \frac{1}{2}\sum_{s=1}^{+\infty}\hat{G}_s^{pq}(\xi) \\ \times\left\{I_{\frac{n-2}{2}}(b)\left[J_{n-s}(a)J_{2-s}(c)+J_{n+s}(a)J_{2+s}(c)\right](-1)^s\right. \\ \left.+I_{\frac{n+2}{2}}(b)\left[J_{n-s}(a)J_{2+s}(c)+J_{n+s}(a)J_{2-s}(c)\right]\right\} \quad n \text{ even; 0 otherwise.} \end{aligned} \tag{43}$$

Equation (34) becomes

$$\sigma_{12,n}^{pq}(\theta;u) = 2A\pi e^{-Q_z^2\sigma_\eta^2}\int_0^\infty\int_0^\infty r\,d\xi\,dr \times \Big(\hat{W}_0(\xi)\Big\{e^{Q_z^2 W_0(r)}\big[\text{Equation (42)} - \hat{G}_0^{pq}(\xi)I_{\frac{n}{2}}(b)J_n(a)\big] + \hat{G}_0^{pq}(\xi)J_0(a)\delta_{n,0}\Big\} + \hat{W}_2(\xi)\times\Big\{e^{Q_z^2 W_0(r)}\big[\text{Equation (43)} - \hat{G}_2^{pq}(\xi)\sum_{\gamma=\pm1} J_{n\gamma+2}(a)I_{\frac{n\gamma+2}{2}}(b)\big] + \hat{G}_2^{pq}(\xi)J_0(a)\delta_{n,\pm2}\Big\}\Big), \quad n \text{ even.} \tag{44}$$

Eventually, from Equation (34), the computation of the BNRCS $\sigma_{12,n}^{pq}$ requires two-fold numerical integrations over the radial distance r and the wavenumber ξ, and one numerical integration over $\phi_\xi - \nu\phi$ for the calculation of the Fourier series coefficients defined by Equation (33). In addition, a sum is required for the computation of the SSA2.

4. Numerical results

For incidence angles of interest for remote sensing applications, $\theta \in [0; 60]$ degrees, and for the VV and HH co-polarizations, this section presents numerical results of the incoherent BNRCS by assuming an anisotropic height spectrum given by the Elfouhaily et al. [36] model. Two radar frequencies are studied, $f = 5.3$ GHz (C-band, sea relative permittivity $\epsilon_r = 67 + j35$ [39]) and $f = 14$ GHz (Ku-band, $\epsilon_r = 47 + j38$ [39]).

The numerical evaluations of the BNRCSs $\{\sigma_{11,0}^{pq}, \sigma_{11,2}^{pq}\}$ given by Equation (28) are rather simple. First, the isotropic $W_0(r)$ and anisotropic $W_2(r)$ parts of the correlation function are computed over $r \in [0; r_{\max}]$ from Equations (26). For frequencies $f = \{5.3, 14\}$ GHz, the maximum radial distance is $r_{\max} \approx \{5, 1\}$ meters. It decreases when the incidence angle decreases, the wind speed increases and the frequency increases. In fact, $r_{\max}$ is a decreasing function of the Rayleigh roughness parameter defined as $R_a = Q_z^2\sigma_\eta^2 = 4\sigma_\eta^2\cos^2\theta\,(2\pi f/c)^2$ with $c = 3\times10^8$ m/s. It is important to note that since the sea correlation function is independent of $\{\theta, f\}$, $\{W_0(r), W_2(r)\}$ were computed and stored in a data file. In addition, the sampling over the radial distance r is done in a *logarithmic* scale with 200 samples.

The numerical evaluations of the BNRCSs $\{\sigma_{12,0}^{pq}, \sigma_{12,2}^{pq}\}$ given by Equation (34) are more complicated, because they require an additional integration over the sea wavenumber $\xi \in [\xi_{\min}; \xi_{\max}]$. We choose $\xi_{\min} = 0.25k_p$, which corresponds to the value for which the sea height isotropic spectrum falls down to 10^{-5} times its maximum, which occurs at k_p. The value $\xi_{\max}$ equals $4K = 8\pi f/c$. Thus, the double integration over $r \in [0; r_{\max}]$ and over $\xi \in [\xi_{\min}; \xi_{\max}]$ is done in a *logarithmic* scale with 200×200 samples. Finally, the Fourier series coefficients defined by Equation (33) are calculated by using a sampling step over $\phi_\xi - \nu\phi$ of 3 degrees. The BNRCSs require the computation of a sum over s from 0 to $s_{\max}$ (see Equations (42) and (43) of the SSA2 model). With the LCA model, $s_{\max} = 0$, whereas for the SSA model, $s_{\max}$ must be determined. This aspect will be presented in Subsection 4.2. For VV polarization, The SSA2 kernel may present singular behaviour when the modulus of the sea relative permittivity is much greater than 1 (it tends to a perfectly conducting surface). For the simulations presented in this paper, this is not the case.

With these parameters, for a given incidence angle θ, on a PC with 4GB of RAM and a processor of 3 GHz, the computing time is of the order of 0.9 second. The scope of the paper is not to compare the different backscattering models with measurements. This was already done thoroughly in previous work [21–23,25–27].

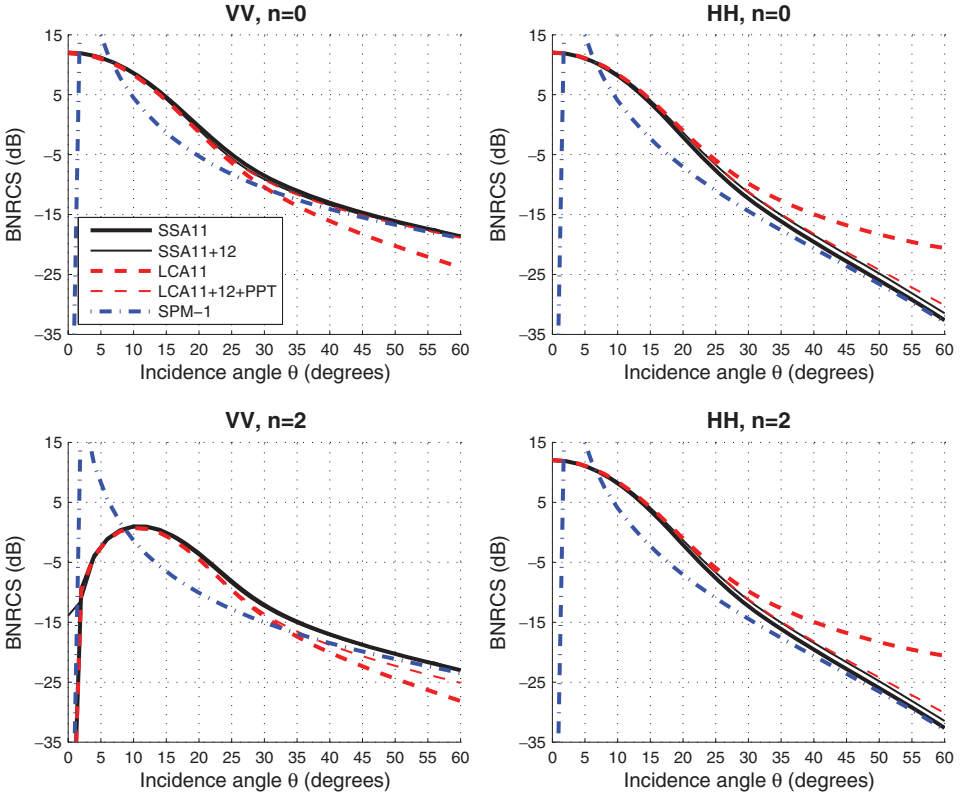

Figure 1. BNRCS versus the incidence angle θ for $f = 14$ GHz and $u_{10} = 10$ m/s. At the top $n = 0$ (zero-order harmonic) and at the bottom, $n = 2$ (second-order harmonic). On the left, VV polarization and on the right, HH polarization.

4.1. *Comparison of SSA2, LCA2 and SPM1*

Figure 1 plots the harmonics of the BNRCS versus the incidence angle θ for $f = 14$ GHz, $u_{10} = 10$ m/s and for VV and HH polarizations. The labels in the legend mean

- SSA11 corresponds to $\sigma_{11,n}^{pq}$ computed from the SSA-1 model with $n = \{0, 2\}$ and $pq = \{VV, HH\}$,
- SSA11+12 corresponds to $\sigma_{11,n}^{pq} + \sigma_{12,n}^{pq}$ computed from the SSA2 model with $n = \{0, 2\}$ and $pq = \{VV, HH\}$,
- LCA11 corresponds to $\sigma_{11,n}^{pq}$ computed from the LCA-1 model with $n = \{0, 2\}$ and $pq = \{VV, HH\}$,
- LCA11+12+PPT corresponds to $\sigma_{11,n}^{pq}$ computed from the LCA2 model combined with the PPT with $n = \{0, 2\}$ and $pq = \{VV, HH\}$,
- SPM-1 corresponds to $\sigma_{11,n}^{pq}$ computed from the SPM-1 and given by

$$\begin{cases} \sigma_{11,0}^{pq}(\theta; u) = 2\left|\mathcal{N}_1^{pq}(\theta)\right|^2 \hat{W}_0(k_{\mathrm{B}})/k_{\mathrm{B}} \\ \sigma_{11,2}^{pq}(\theta; u) = \sigma_{11,0}^{pq}(\theta; u)\hat{\Delta}(k_{\mathrm{B}}). \end{cases} \tag{45}$$

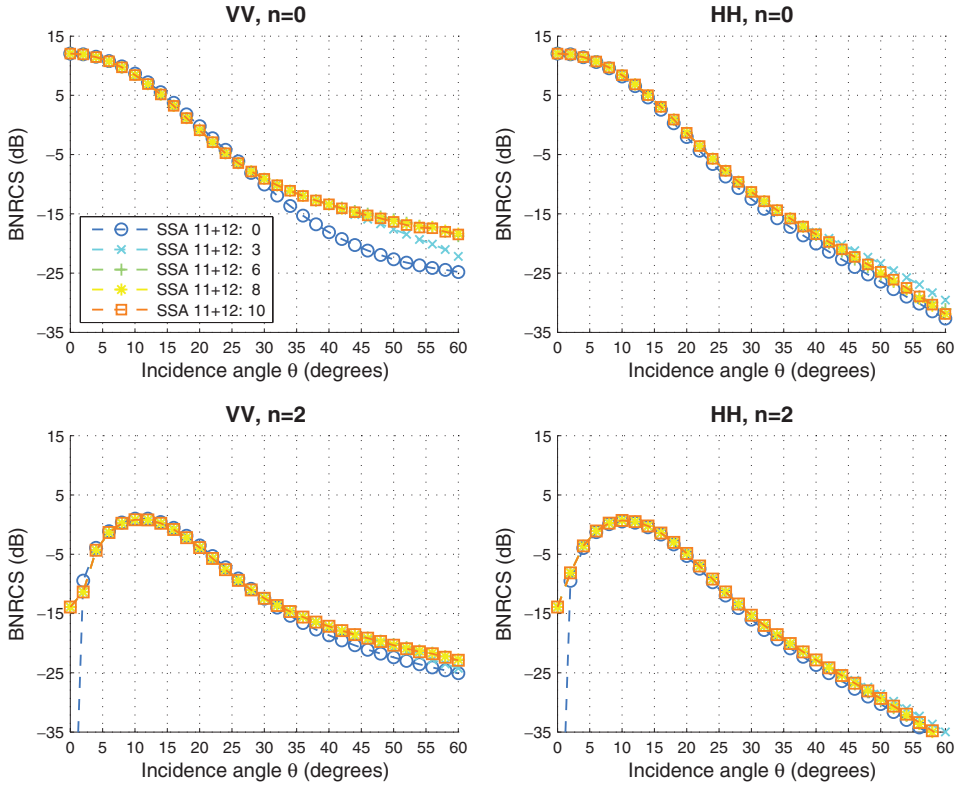

Figure 2. $\sigma_{11,n}^{pq} + \sum_{s=0}^{s=S} \sigma_{12,n}^{pq,s}$ of the SSA2 model versus the incidence angle θ, with different values of the integer S, for $f = 14$ GHz and $u_{10} = 10$ m/s. At the top, $n = 0$ (zero-order harmonic) and at the bottom, $n = 2$ (second-order harmonic). On the left, VV polarization and on the right, HH polarization.

As expected, the BNRCS decreases more quickly for HH polarization. For near-nadir incidence angles, Figure 1 reveals that the LCA11 and the SSA11 models are similar, which means that SSA11 reproduces the KA-1 reduced to the SPA (theoretically, SSA11 does not reproduce the Kirchhoff approximation, but since the sea surface is highly conducting and the backscattering angle vanishes, the SPM polarization matrix is close to the Kirchhoff one). It can be noted that by construction, the LCA11 model is the same as the KA-1 + SPA model. For incidence angles ranging from 0 to approximately 20 degrees, only gravity waves contribute to the scattering and therefore KA-1 + SPA can be applied. However, a smooth transition for scattering angles $\theta \in [20; 40]$ degrees is observed, for which the KA-1+SPA model becomes invalid and the Bragg scattering regime (given by SPM1) contributes increasingly. In this region, SSA11 tends to SPM1, and the higher orders of SSA2 and LCA2 contribute. For the LCA2 model, this contribution is positive for the VV polarization, whereas it is negative for the HH polarization. For the SSA2 model, this contribution is negative for the VV polarization and it is weak, whereas it is positive for the HH polarization and it is much smaller than that of the LCA model. Thus, the behaviour of the kernel of each model is very different.

It is important to note that the LCA2 results plotted in Figure 1 use the PPT, which consists in adding the term $|\hat{\mathcal{N}}_2^{pq}|^2$ in Equation (31). If the PPT is not applied, then for larger scattering angles, simulations, not reported in this paper, show a non-physical behaviour of the BNRCS

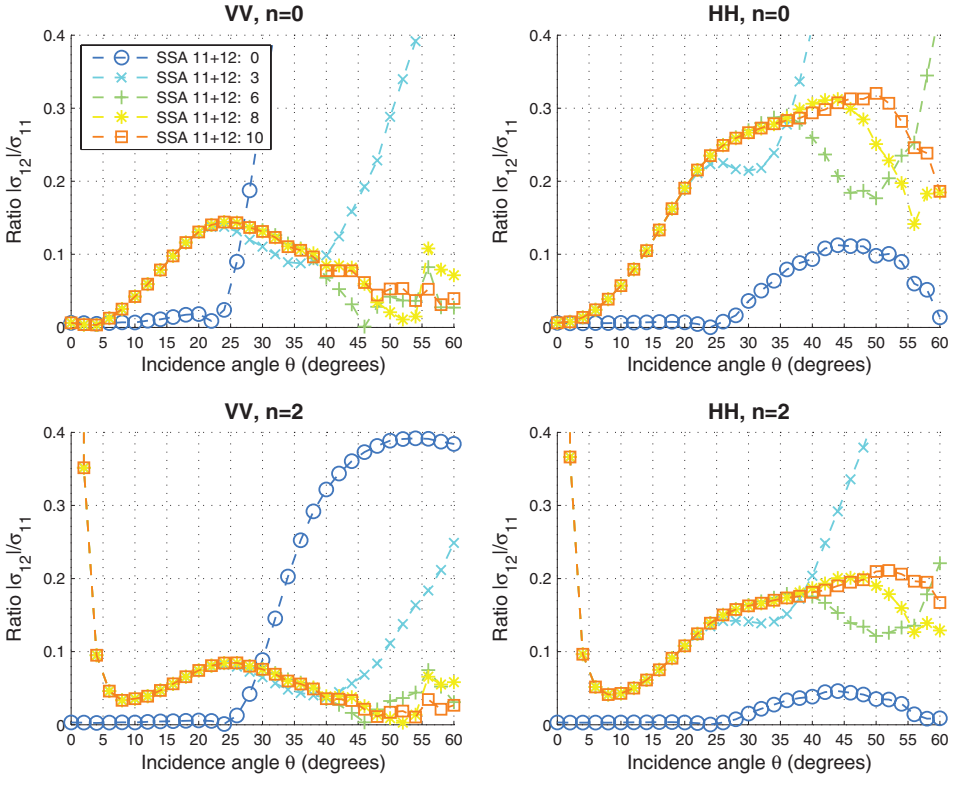

Figure 3. Ratio $|\sum_{s=0}^{s=S}\sigma_{12,n}^{pq,s}|/\sigma_{11,n}^{pq}$ of the SSA2 model versus the incidence angle θ, with different values of the integer S, for $f = 14$ GHz and $u_{10} = 10$ m/s. At the top, $n = 0$ (zero-order harmonic) and at the bottom, $n = 2$ (second-order harmonic). On the left, VV polarization and on the right, HH polarization.

for the HH polarization. With the SSA model, the results obtained with the PPT are the same as those plotted in Figure 1. For a one-dimensional sea surface, as explained in detail in the paper of Bourlier et al. [18], although the LCA kernel reaches the SPM1 and the KA1 + SPA limits and is tilt invariant, the BNRCS does not converge toward the Bragg regime. A theoretical explanation is given in the conclusion of [18]. Thus, the use of the PPT in the LCA model allows us to remove this drawback. This is why, in the paper of Mouche et al. [27], the LCA model with the PPT gives satisfactory results on the BNRCS.

4.2. *Calculation of the integer* $s_{\max}$

In Equations (42) and (43), the sums over $s \in \mathbb{N}$ must be truncated at $s_{\max}$. To compute rigorously the integer $s_{\max}$, the following ratio is defined

$$\kappa = \frac{\sigma_{11,n}^{pq} + \sum_{s=0}^{s=s_{\max}} \sigma_{12,n}^{pq,s}}{\sigma_{11,n}^{pq} + \sigma_{12,n}^{pq}}, \tag{46}$$

where $\sigma_{11,n}^{pq,s}$ is the elementary BNRCS at order s of $\sigma_{12,n}^{pq} = \sum_{s=0}^{s=\infty}\sigma_{12,n}^{pq,s}$ ($s_{\max} \to \infty$). As the integer $s_{\max}$ increases, the ratio κ converges toward 1. From the above equation, $s_{\max}$ is then

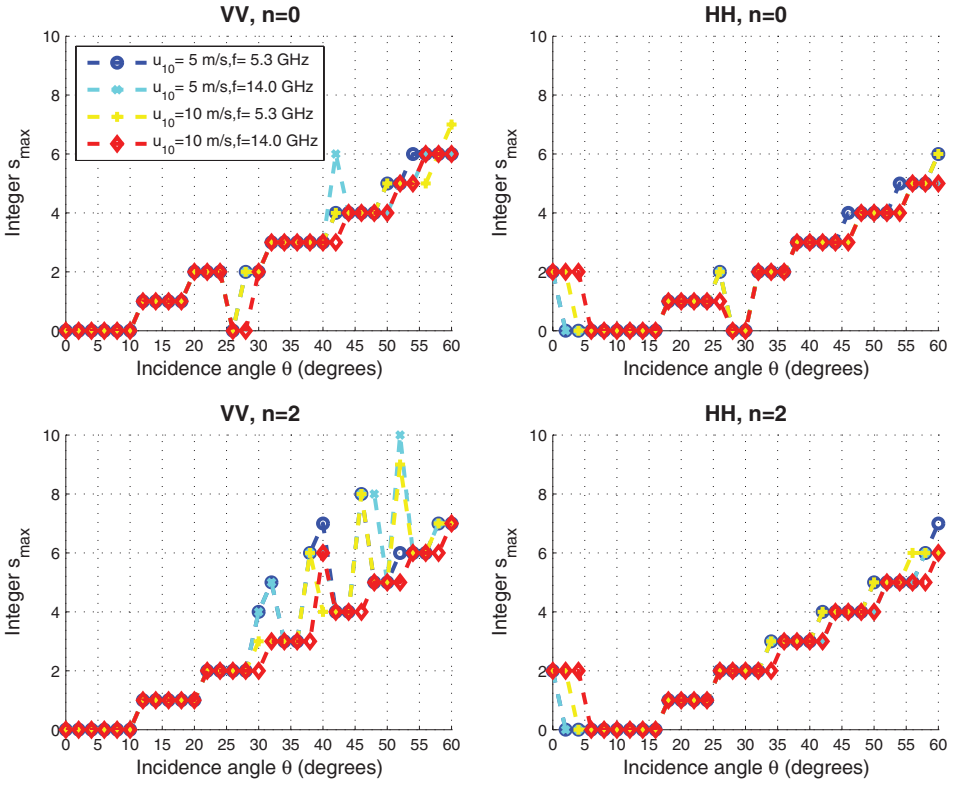

Figure 4. Integer $s_{\max}$ of the SSA model versus the incidence angle θ for frequencies $f = \{5.3, 14\}$ GHz and for wind speeds $u_{10} = \{5, 10\}$ m/s. At the top, $n = 0$ (zero-order harmonic) and at the bottom, $n = 2$ (second-order harmonic). On the left, VV polarization and on the right, HH polarization.

obtained when κ becomes larger than a threshold $\kappa_s \in]0; 1[$. For the simulation $\kappa_s = -0.3$ dB, corresponding to $\kappa_s = 0.933$ in linear scale.

Figure 2 plots the BNRCS $\sigma_{11,n}^{pq} + \sum_{s=0}^{s=S} \sigma_{12,n}^{pq,s}$ for increasing $S \in [0; s_{\max}]$ of the SSA2 model versus the incidence angle θ, for $f = 14$ GHz and $u_{10} = 10$ m/s. To better see the difference according to S, Figure 3 plots the ratio $|\sum_{s=0}^{s=S} \sigma_{12,n}^{pq,s}|/\sigma_{11,n}^{pq}$. As can be seen, for increasing S, the difference with the next integration $S + 1$ decreases, and then the difference becomes negligible when $S = s_{\max}$.

Figure 4 plots the integer $s_{\max}$ of the SSA2 model versus the incidence angle θ, for frequencies $f = \{5.3, 14\}$ GHz and for wind speeds $u_{10} = \{5, 10\}$ m/s. As can be seen, the integer $s_{\max}$ increases slightly with the angle θ, and is not very sensitive to the polarization and the order n of the harmonic. Typically, for $\theta \leq 30$ degrees, $s_{\max} \leq 3$, whereas for $\theta \in]30; 60]$ degrees, $s_{\max}$ reaches the maximum value 7 on average. Thus, the sum over s converges rapidly.

4.3. *Optimization of the SSA2 and LCA2 computation*

Equation (34) requires the computation of two-fold numerical integrations over the radial distance r and the sea wavenumber ξ. First, integrating over r, the resulting integrand depends then only on ξ. Plotting this integrand versus ξ, we observe that two wavenumbers $\{\xi_l, \xi_h\}$ mainly contribute to the scattering process. The first one is defined as $\xi_l = 1.66k_p$ (low frequency), in which k_p

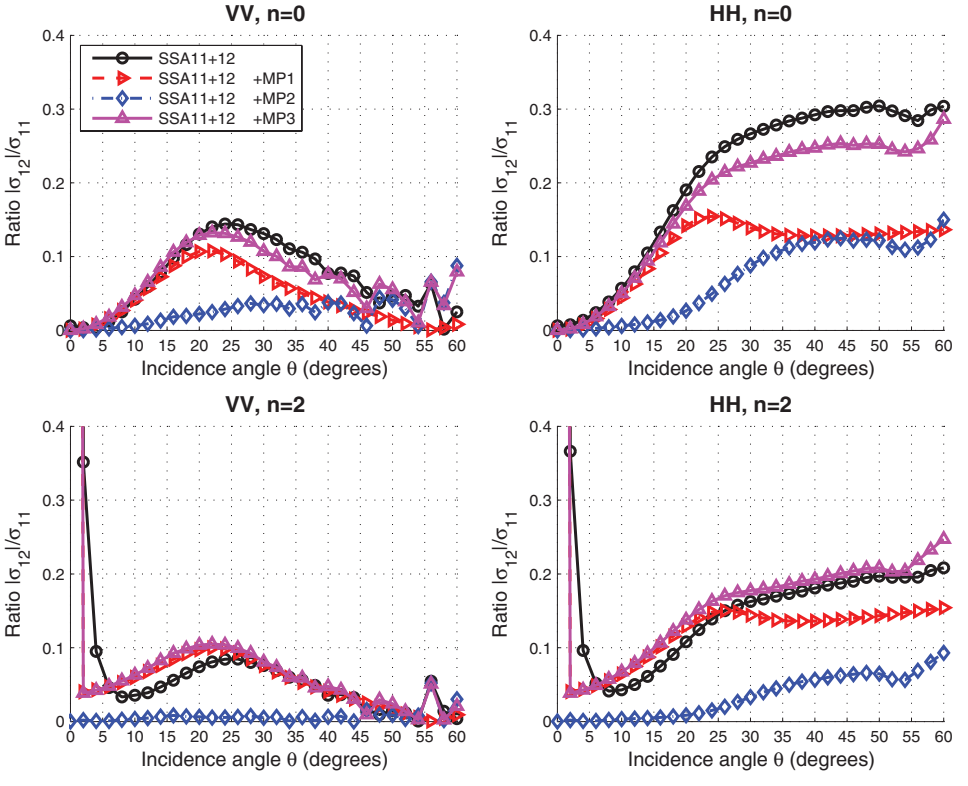

Figure 5. Ratio $|\sigma_{12,n}^{pq}|/\sigma_{11,n}^{pq}$ of the SSA model versus the incidence angle θ, with different choices of the integration over ξ. At the top, $n = 0$ (zero-order harmonic) and at the bottom, $n = 2$ (second-order harmonic). On the left, VV polarization and on the right, HH polarization.

corresponds to the wavenumber for which the sea *height* isotropic spectrum $\hat{W}_0(\xi)$ is maximum. In fact, $1.66k_p$ corresponds to the maximum of the *slope* isotropic spectrum $\xi^2\hat{W}_0(\xi)$. The second one is defined as $\xi_h = k_\mathrm{B}$ (high frequency). Thus, the second-order BNRCS results from the interference of two waves of wavenumbers $\{\xi_l, \xi_h\}$. More precisely, for $\xi = \xi_h$, one can observe that the adjacent wavenumbers also contribute to the scattering process, and we show that $\xi_h \to \xi_h \in [k_\mathrm{B} - \Delta_\xi; k_\mathrm{B} + \Delta_\xi]$, with $\Delta_\xi = 0.5k_\mathrm{B}$. It is equivalent to multiplying the sea spectrum by a pulse function centred around k_B and of width $2\Delta_\xi$.

Figure 5 plots the ratio $|\sigma_{12,n}^{pq}|/\sigma_{11,n}^{pq}$ of the SSA2 model versus the incidence angle θ, with different choices of the integration over ξ. The labels in the legend mean that

- for MP1, $\xi = \xi_l = 1.66k_p$ for the integration,
- for MP2, $\xi = \xi_h$ for the integration with a sampling step of $0.1k_\mathrm{B}$ ($n_\xi = 11$),
- for MP3, $\xi = \{\xi_l, \xi_h\}$ for the integration,
- else $\xi \in [0.25k_p; 4K]$ (full spectrum) with $n_\xi = 200$ (number of samples).

As one can see, for low incidence angles, only the sea wavenumber $\xi = \xi_l$ contributes to the scattering process, whereas for moderate incidence angles (Bragg regime), both the low (ξ_l) and high frequencies ($\{\xi_h\}$) contribute. Moreover, the results are very close to that obtained from the

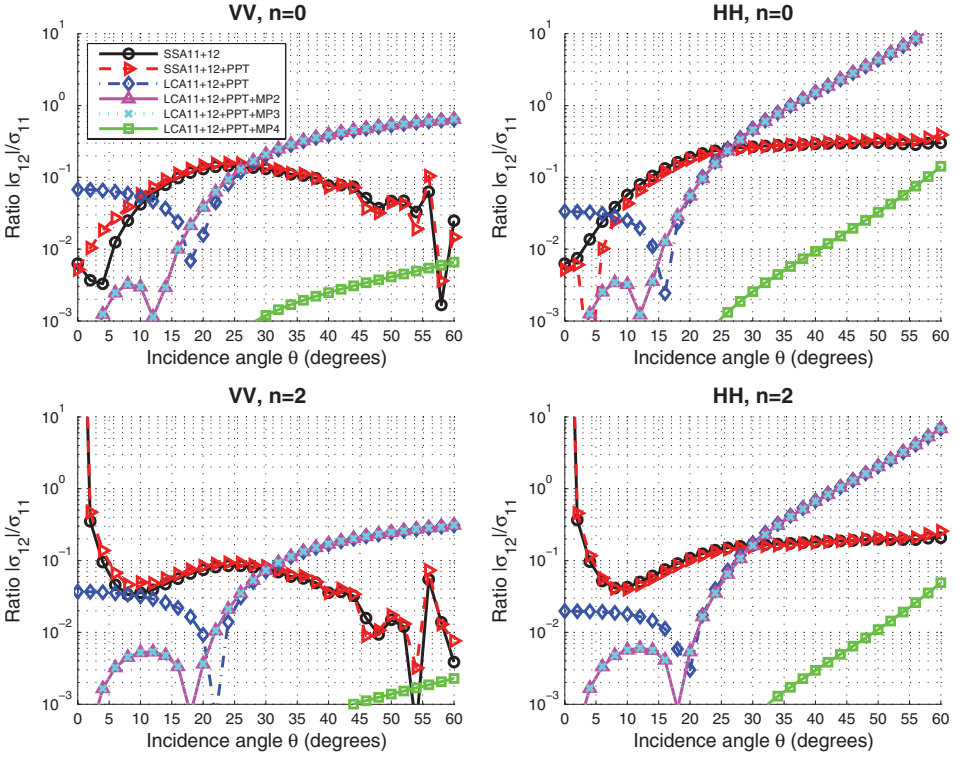

Figure 6. Ratio $|\sigma_{12,n}^{pq}|/\sigma_{11,n}^{pq}$ of different kernels versus the incidence angle θ, with different choices of the integration over ξ. At the top, $n = 0$ (zero-order harmonic) and at the bottom, $n = 2$ (second-order harmonic). On the left, VV polarization and on the right, HH polarization.

full spectrum. Thus, with this new integration, the computing time is reduced to 0.07 second instead of 0.90 second, when the full spectrum is used.

Figure 6 plots the ratio $|\sigma_{12,n}^{pq}|/\sigma_{11,n}^{pq}$ of the SSA and LCA models with and without the inclusion of the PPT versus the incidence angle θ, and with different choices of the integration over ξ for the LCA model. The model with the label 'LCA11 + 12 + PPT + MP4' is *similar* (but not equivalent) to the reduced curvature approximation (RCA) model developed by Mouche et al. [27]. It only includes the Bragg frequency $\xi = k_B$, whereas the model with the label 'LCA11 + 12 + PPT + MP2' includes the frequencies $\xi \in [k_B - \Delta_\xi; k_B + \Delta_\xi]$ with $\Delta_\xi = 0.5k_B$ for the integration over ξ.

As one can see, for the SSA model, the results with and without the PPT are similar. The LCA results show that the low frequencies contribute to the scattering process only for incidence angles smaller than 25 degrees, since the results with the labels 'MP2' ($\xi = \xi_h$, high-frequency component) and 'MP3' ($\xi = \{\xi_l, \xi_h\}$, low- and high-frequency components) become similar for $\theta > 25^\circ$. In addition, since $\sigma_{12} \ll \sigma_{11}$ for small θ angles, we can conclude for $\theta \in [0; 60]^\circ$ that the LCA11 + 12 + PPT model gives similar results to the LCA11 + 12 + PPT + MP2 one. When only a single wavenumber $\xi = k_B$ is taken into account in the integration over ξ (label 'LCA11 + 12 + PPT + MP4'), the BNRCS is underestimated. This behaviour does not occur in the paper of Mouche et al. [27]. A possible explanation is that they used the approximation $1 + x \approx e^x$, which implies that the BNRCS is overpredicted since $e^x \geq 1 + x \ \forall x$, and thus a single frequency is sufficient to model the Bragg modulation, whereas several frequencies around $\xi = k_B$ are needed when the approximation $1 + x \approx e^x$ is not applied.

The different behaviour of the SSA and LCA models can be explained by the fact that the LCA2 sub-kernel is quadratic in its lowest order ($\hat{\mathcal{N}}_2^{pq}(\boldsymbol{\xi}) = [\boldsymbol{\nabla}\boldsymbol{\nabla}\hat{\mathcal{N}}_2^{pq}(\boldsymbol{\xi})]_{\boldsymbol{\xi}=\mathbf{0}}\,\boldsymbol{\xi}^2 + \mathcal{O}(\boldsymbol{\xi}^2)$), whereas the SSA2 sub-kernel behaves as $\hat{\mathcal{N}}_2^{pq}(\boldsymbol{\xi}) = [\boldsymbol{\nabla}\hat{\mathcal{N}}_2^{pq}(\boldsymbol{\xi})]_{\boldsymbol{\xi}=\mathbf{0}}\,\boldsymbol{\xi} + \mathcal{O}(\boldsymbol{\xi})$. Thus, the SSA model brings more low-frequency components than the LCA model, which explains that in Figure 5, the curve with the label 'MP1' ($\xi = \xi_l$, low-frequency component) is comparable to the curve with the label 'MP3' ($\xi = \{\xi_l, \xi_h\}$, low- and high-frequency components). This is not the case for the LCA2 model, because the LCA1 kernel reaches the KA-1+SPA limit, whereas the SSA1 kernel reaches the SPM-1 limit, and thus, its higher order, SSA2, must compensate this behaviour to reach the KA-1+SPA limit for small incidence angles θ.

5. Conclusion

In this paper, closed-form expressions of the Fourier coefficients $\sigma_n(\theta, u_{10})$ along $\cos(n\phi)$ of the BNRCS are expressed. Since a Gaussian process is assumed, $\sigma_1 = 0$. Then, the '11' order, resulting from the correlation of the first-order scattered field, requires two independent numerical integrations over the wavenumber ξ (for the calculation of the height correlation function), and over the radial distance r. The '12' order, resulting from the cross-correlation between the first- and second-order scattered fields, requires two-fold numerical integrations over the radial distance r and over the wavenumber ξ, and one numerical angular integration for the computation of the Fourier series coefficients of the second-order kernel. The SSA2 and LCA2 kernels were tested for microwaves frequencies and different wind speeds. The numerical results showed that the SSA2 and LCA2 have different behaviours, and the correction from the '12' order is larger for the LCA2 model than for the SSA2 model. In addition, an optimization for the numerical integration over ξ was proposed, leading to a computing time of the '12' order less than 0.1 second on a standard office computer for a given wind speed, a given frequency and a given incidence angle.

The prospects of this paper are the extension of the formulation to a non-Gaussian process, as done in [23] for the '11' order, and the calculation of the BNRCS for the cross-polarizations with the help of the PPT. Indeed, if the PPT is not used, the '12' order contribution vanishes because in Equation (31), $\mathcal{N}_1^{pq} = 0$ in the backscattering direction for $pq = \{HV, VH\}$. In addition, more recent kernels, like the reduced local curvature approximation (RLCA) [10,20], could be implemented.

Acknowledgement

The authors thank the reviewers for their relevant comments, which influenced the final appearance of the paper.

References

[1] B.F. Kur'yanov, *The scattering of sound at a rough surface with two types of irregularity*, Sov. Phys. Acoust. 8 (1963), pp. 252–257.
[2] J.W. Wright, *A new model for sea clutter*, IEEE Trans. Ant. Prop. 16 (1968), pp. 217–223.
[3] G. Soriano and C.-A. Guérin, *A cutoff invariant two-scale model in electromagnetic scattering from sea surfaces*, IEEE Trans. Geos. Rem. Sensing Lett. 5 (2008), pp. 199–203.
[4] N. Sajjad, A. Kenchaf, A. Coathanay, and A. Awada, *An improved two-scale model for the ocean surface bistatic scattering*. Paper presented at the International Geoscience and Remote Sensing Symposium, Boston, MA, 2008.
[5] S. Boukabara, L. Eymard, C. Guillou, D. Lemaire, P. Sobieski, and A. Guissard, *Development of a modified two-scale electromagnetic model simulating both active and passive microwave measurements: Comparison to data remotely sensed over the ocean*, Radio Sci. 37 (2002), pp. 1063–1073.

[6] T.M. Elfouhaily and C.-A. Guérin, *A critical survey of approximate scattering wave theories from random rough surfaces*, Waves Random Complex Media 14 (2006), pp. R1–R40.
[7] A.G. Voronovich, *Small slope approximation for electromagnetic wave scattering at a rough interface of two dielectric half-spaces*, Waves Random Complex Media 4 (1994), pp. 337–367.
[8] A.G. Voronovich, *Wave Scattering from Rough Surfaces*, 2nd ed., Springer Series on Wave Phenomena, Springer-Verlag, Berlin, 1999.
[9] T.M. Elfouhaily, S. Guignard, R. Awadallah, and D.R. Thompson, *Local and non-local curvature approximation: A new asymptotic theory for wave scattering*, Waves Random Complex Media 13 (2003), pp. 321–337.
[10] T.M. Elfouhaily and J.T. Johnson, *Extension of the local curvature approximation to third order and full tilt invariance*, *Waves Random Complex Media* 16 (2006), pp. 97–119.
[11] G. Soriano, C.A. Guérin, and M. Saillard, *Scattering by two-dimensional rough surface: Method comparison*, Waves Random Complex Media 12 (2002), pp. 63–83.
[12] S.L. Broschat and E.I. Thorsos, *An investigation of the small slope approximation for scattering from rough surfaces. Part II. Numerical studies*, J. Acoust. Soc. Am. 101 (1997), pp. 2615–2625.
[13] G. Berginc, *Small-slope approximation method: A further study of vector wave scattering from two-dimensional surfaces and comparison with experimental data*, Prog. Electromag. Res. 37 (2002), pp. 251–287.
[14] M.S. Gilbert and J.T. Johnson, *A study of the higher-order small-slope approximation for scattering from a Gaussian rough surface*, Waves Random Complex Media 13 (2003), pp. 137–149.
[15] C.A. Guérin, G. Soriano, and T.M. Elfouhaily, *Weighted curvature approximation: Numerical tests for 2D dielectric surfaces*, Waves Random Complex Media 14 (2003), pp. 349–363.
[16] J.T. Johnson, *A numerical study of low-grazing-angle backscatter from ocean-like impedance surfaces with the canonical grid method*, IEEE Trans. Ant. Prop. 46 (1998), pp. 114–120.
[17] H. Kim and J.T. Johnson, *Radar image studies of an ocean-like surface*, Microwave Opt. Tech. Lett. 30 (2001), pp. 381–384.
[18] C. Bourlier, N. Déchamps, and G. Berginc, *Comparison of asymptotic backscattering models (SSA, WCA, and LCA) from one-dimensional gaussian ocean-like surfaces*, IEEE Trans. Ant. Prop. 53 (2005), pp. 1640–1652.
[19] J.T. Johnson, *A study of ocean-like surface thermal emission and reflection using Voronovich's small slope approximation*, IEEE Trans. Geos. Rem. Sensing 43 (2005), pp. 306–314.
[20] J.T. Johnson and T.M. Elfouhaily, *Computation of ocean-like surface thermal emission and bistatic scattering with the reduced local curvature approximation*, IEEE Trans. Geos. Rem. Sensing 45 (2007), pp. 2108–2115.
[21] V. Voronovich, V. Zavorotny, and V.G. Irisov, *Sea-roughness spectrum retrieval from radar and radiometric measurements*. Paper presented at the International Geoscience and Remote Sensing Symposium, Piscataway, NJ, 2000.
[22] C. Bourlier and G. Berginc, *Microwave analytical backscattering models from randomly rough anisotropic sea surface – Comparison with experimental data in C and Ku bands*, Prog. Electromag. Res. 37 (2002), pp. 31–78.
[23] C. Bourlier, *Azimuthal harmonic coefficients of the microwave backscattering from a non-Gaussian ocean surface with the first-order SSA model*, IEEE Trans. Geos. Rem. Sensing 42 (2004), pp. 2600–2611.
[24] A. Awada, M.Y. Ayari, A. Khenchaf, and A. Coatanhay, *Bistatic scattering from an anisotropic sea surface: Numerical comparison between the first-order SSA and the TSM models*, Waves Random Complex Media 16 (2006), pp. 383–394.
[25] S.T. McDaniel, *Small-slope predictions of microwave backscatter from the sea surface*, Waves Random Complex Media 11 (2001), pp. 343–360.
[26] A.G. Voronovich and V.U. Zavorotny, *Theoretical model for scattering of radar signals in Ku- and C-bands from a rough sea surface with breaking waves*, Waves Random Complex Media 11 (2001), pp. 247–269.
[27] A.A. Mouche, B. Chapron, and N. Reul, *A simplified asymptotic theory for ocean surface electromagnetic wave scattering*, Waves Random Complex Media 17 (2007), pp. 321–341.
[28] F.J. Wentz, S. Peteherich, and L.A. Thomas, *A model function for ocean radar cross section at 14.6 GHz*, J. Geo. Res. 89 (1984), pp. 3689–3704.

[29] M. Masuko, K. Okamoto, M. Shimada, and S. Niwa, *Measurements of microwave bsckscattering signatures of the oecan surface using X band ang Ka Band airbone scatterometers*, J. Geo. Res. 91 (1986), pp. 13065–13088.
[30] S.V. Nghiem, F.K. Li, and G. Neumann, *The dependence of ocean backscatter at Ku-band on oceanic and atmospheric parameters*, *IEEE Trans. Geos. Rem. Sens.* 35 (1997), pp. 581–600.
[31] Y. Quilfen, B. Chapron, T. Elfouhaily, K. Katsaros, and J. Tournadre, *Observation of tropical cyclones by high resolution scatterometry*, J. Geo. Res. 103 (1998), pp. 7767–7786.
[32] A. Bentamy, P. Queffeulou, Y. Quilfen, and K. Katsaros, *Ocean surface wind fields estimated from satellite active and passive microwave instruments*, IEEE Trans. Geos. Rem. Sens. 37 (1999), pp. 2469–2486.
[33] F.J. Wentz and D. K. Smith, *A model function for ocean-normalized radar cross section at 14 GHz derived from NSCAT observations*, J. Geo. Res. 104 (1999), pp. 11499–11514.
[34] A.A. Mouche, D. Hauser, J.-F. Daloze, and C. Guerin, *Dual-polarization measurements at C band over the ocean: Results from airborne radar observations and comparison with ENVISAT ASAR data*, IEEE Trans. Geos. Rem. Sens. 43 (2005), pp. 753–769.
[35] C.-A. Guérin and M. Saillard, *On the high-frequency limit of the second-order small-slope approximation*, Waves Random Complex Media 13 (2003), pp. 75–88.
[36] T. Elfouhaily, B. Chapron, K. Katsaros, and D. Vandemark, *A unified directional spectrum for long and short wind-driven waves*, J. Geo. Res. 102 (1997), pp. 781–796.
[37] M. Abramowitz and I.A. Segun, *Handbook of Mathematical Functions*, Dover Publications, New York, 1972.
[38] I.S. Gradshteyn and I.M. Ryzhik, *Table of Integrals, Series, and Products*, Academic Press, New York, 2000.
[39] W. Ellison, A. Balana, G. Delbos, K. Lamkaouchi, L. Eymard, C. Guillou, and C. Prigent, *New permittivity measurements of seawater*, Radio Sci. 33 (1998), pp. 639–648.

Appendix 1. Derivation of the statistical average

From Equation (9), with $\eta(\mathbf{r}_i) = \eta_i$, one has

$$\left\langle \mathcal{N}_2^{pq}(\mathbf{r}_2) e^{jQ_z(\eta_1-\eta_2)} \right\rangle = \left\langle \int_{\boldsymbol{\xi}_2} \hat{\mathcal{N}}_2^{pq}(\boldsymbol{\xi}_2)\hat{\eta}(\boldsymbol{\xi}_2) e^{j\boldsymbol{\xi}_2\cdot\mathbf{r}_2} e^{jQ_z(\eta_1-\eta_2)} d\boldsymbol{\xi}_2 \right\rangle$$
$$= \frac{1}{(2\pi)^2} \int_{\boldsymbol{\xi}_2}\int_{\mathbf{r}_3} \hat{\mathcal{N}}_2^{pq}(\boldsymbol{\xi}_2) e^{j\boldsymbol{\xi}_2\cdot(\mathbf{r}_2-\mathbf{r}_3)} \left\langle \eta_3 e^{jQ_z(\eta_1-\eta_2)} \right\rangle d\boldsymbol{\xi}_2 d\mathbf{r}_3, \tag{47}$$

where $\hat{\eta}(\boldsymbol{\xi}_2) = \frac{1}{(2\pi)^2}\int_{\mathbf{r}_3} \eta_3 e^{-j\boldsymbol{\xi}_2\cdot\mathbf{r}_3} d\mathbf{r}_3$. Thus, the calculation of the statistical average requires the derivation of $\left\langle \eta_3 e^{jQ_z(\eta_1-\eta_2)} \right\rangle$. To do so, the following property is applied

$$\eta_3 e^{jQ_z(\eta_1-\eta_2)} = \left[\frac{\partial}{\partial a_3} e^{jQ_z(\eta_1-\eta_2)+a_3\eta_3} \right]\Bigg|_{a_3=0}. \tag{48}$$

Since $\langle e^{\eta}\rangle = e^{\langle\eta^2\rangle/2}$ and the sum of Gaussian random variables is also a Gaussian random variable, Equation (48) can be expanded as

$$\left\langle \eta_3 e^{jQ_z(\eta_1-\eta_2)} \right\rangle = jQ_z \left\langle e^{jQ_z(\eta_1-\eta_2)} \right\rangle [W(\mathbf{r}_{13}) - W(\mathbf{r}_{23})], \tag{49}$$

where $\langle e^{jQ_z(\eta_1-\eta_2)}\rangle$ is expressed from Equation (14), and W is the height correlation function.

Noting that the integral (47) depends only on $\mathbf{r}_2 - \mathbf{r}_3 = -\mathbf{r}_{23}$, the substitution of (49) into (47) yields

$$\left\langle \mathcal{N}_2^{pq}(\mathbf{r}_2) e^{jQ_z(\eta_1-\eta_2)} \right\rangle = jQ_z \left\langle e^{jQ_z(\eta_1-\eta_2)} \right\rangle \left[W_m^{pq}(\mathbf{r}) - W_m^{pq}(\mathbf{0}) \right], \tag{50}$$

where

$$W_m^{pq}(\mathbf{r}) = \int_{\boldsymbol{\xi}} \hat{\mathcal{N}}_2^{pq}(\boldsymbol{\xi}) \hat{W}(\boldsymbol{\xi}) e^{j\boldsymbol{\xi}\cdot\mathbf{r}} d\boldsymbol{\xi}, \tag{51}$$

$\hat{W}(\boldsymbol{\xi})$ being the sea spectrum.

Since $\langle \eta_1^* e^{jQ_z(\eta_1-\eta_2)} \rangle = [\langle \eta_2 e^{jQ_z(\eta_1-\eta_2)} \rangle]^*|_{\{1,2\}\to\{2,1\}}$, we eventually have

$$\left\langle \eta_f^*(\mathbf{r}_1) e^{jQ_z(\eta_1-\eta_2)} \right\rangle = -jQ_z \left\langle e^{jQ_z(\eta_1-\eta_2)} \right\rangle \left[W_m^{pq*}(-\mathbf{r}) - W_m^{pq*}(\mathbf{0}) \right]. \tag{52}$$

Appendix 2. Integration over ϕ_r

Let us consider the following integral

$$\Psi_0(a,b,\phi) = \frac{1}{2\pi} \int_0^{2\pi} e^{ja\cos(\phi-\phi_r) - b\cos(2\phi_r)} d\phi_r. \tag{53}$$

The exponential term can be expanded as [37]

$$\begin{cases} \exp[ja\cos(\phi-\phi_r)] = \displaystyle\sum_{n=-\infty}^{n=+\infty} j^n J_n(a) e^{jn(\phi-\phi_r)} \\ \exp[-b\cos(2\phi_r)] = \displaystyle\sum_{m=-\infty}^{m=+\infty} j^m J_m(jb) e^{2jm\phi_r}, \end{cases} \tag{54}$$

where J_m is the Bessel function of the first kind and of order m. Substitution of Equation (54) into Equation (53) and the derivation of the integration over ϕ_r lead to

$$\Psi_0(a,b,\phi) = \sum_{n,m} j^{n+m} J_n(a) J_m(jb) e^{jn\phi} \delta_{2m-n,0}, \tag{55}$$

where $\delta_{n,p}$ is the Kronecker symbol defined as $\delta_{n,p} = 1$ if $n = p$; 0 otherwise. In addition, since $J_m(jb) = j^m I_m(b)$, where I_m denotes the Bessel function of the second kind and of order m, we obtain

$$\begin{aligned} \Psi_0(a,b,\phi) &= \sum_{m=-\infty}^{m=+\infty} J_{2m}(a) I_m(b) e^{2jm\phi} \\ &= J_0(a) I_0(b) + 2 \sum_{m=1}^{m=+\infty} J_{2m}(a) I_m(b) \cos(2m\phi), \end{aligned} \tag{56}$$

because $J_{-2m}(a) = (-1)^{2m} J_{2m}(a) = J_{2m}(a)$ and $I_{-m}(b) = I_m(b)$.

Appendix 3. Backscattering polarization matrices of the SSA2 kernel

In the backscattering direction, the dimensionless elements of the SPM-1 polarization matrix are [7]

$$\begin{cases} \mathcal{B}_1^{VV}(-\mathbf{k}_0, \mathbf{k}_0) = \frac{(1-\epsilon_r)(q_0'^2+\epsilon_r k_0^2)}{(\epsilon_r q_0+q_0')^2} \\ \mathcal{B}_1^{VH}(-\mathbf{k}_0, \mathbf{k}_0) = \mathcal{B}_1^{HV}(-\mathbf{k}_0, \mathbf{k}_0) = 0 \\ \mathcal{B}_1^{HH}(-\mathbf{k}_0, \mathbf{k}_0) = \frac{\epsilon_r-1}{(q_0+q_0')^2} K^2, \end{cases} \tag{57}$$

whereas the elements of the SPM-2 polarization matrix are [7]

$$\begin{cases} \mathcal{B}_2^{VV}(-\mathbf{k}_0, \mathbf{k}_0; \boldsymbol{\xi}) = \frac{2(\epsilon_r-1)}{(\epsilon_r q_0+q_0')^2} \left\{ \frac{1-\epsilon_r}{\epsilon_r q_\xi+q_\xi'} \left[\epsilon_r k_0^2 \xi^2 - q_0'^2 \frac{(\mathbf{k}_0\cdot\boldsymbol{\xi})^2}{k_0^2} \right] \right. \\ \qquad\qquad \left. + q_0'^2 \left(q_\xi - q_\xi'\right) + \epsilon_r K^2 q_\xi' \right\} \\ \mathcal{B}_2^{HH}(-\mathbf{k}_0, \mathbf{k}_0; \boldsymbol{\xi}) = \frac{2(\epsilon_r-1)K^2}{(q_0+q_0')^2} \left\{ \frac{1-\epsilon_r}{\epsilon_r q_\xi+q_\xi'} \left[\xi^2 - \frac{(\mathbf{k}_0\cdot\boldsymbol{\xi})^2}{k_0^2} \right] \right. \\ \qquad\qquad \left. - q_0' - \left(q_\xi - q_\xi'\right) \right\}, \end{cases} \tag{58}$$

with

$$\begin{cases} q_0 = \sqrt{K^2 - k_0^2} \quad q_0' = \sqrt{\epsilon_r K^2 - k_0^2} \\ q_\xi = \sqrt{K^2 - \xi^2} \; q_\xi' = \sqrt{\epsilon_r K^2 - \xi^2}. \end{cases} \tag{59}$$

The elements of the cross-polarizations are not computed and are then not presented. Let us note that the notation $\mathbf{u}^2$ corresponds to $\mathbf{u}^2 = \mathbf{u}\cdot\mathbf{u} = ||\mathbf{u}||^2$. Equation (58) shows that $\mathcal{B}_2^{VV}(-\mathbf{k}_0; \mathbf{k}_0, \boldsymbol{\xi})$ and $\mathcal{B}_2^{HH}(-\mathbf{k}_0, \mathbf{k}_0; \boldsymbol{\xi})$ are even functions with respect to ξ. Thus, in Equation (7) with $\mathbf{k} = -\mathbf{k}_0$, $\mathcal{B}_2^{pq}(-\mathbf{k}_0, \mathbf{k}_0; -\mathbf{k}_0 - \boldsymbol{\xi}) = \mathcal{B}_2^{pq}(-\mathbf{k}_0, \mathbf{k}_0; \mathbf{k}_0 + \boldsymbol{\xi})$, and

$$\begin{aligned} \mathcal{M}^{pq}(-\mathbf{k}_0, \mathbf{k}_0; \boldsymbol{\xi}) &= \mathcal{B}_2^{pq}(-\mathbf{k}_0, \mathbf{k}_0; -\mathbf{k}_0 - \boldsymbol{\xi}) + \mathcal{B}_2^{pq}(-\mathbf{k}_0, \mathbf{k}_0; \mathbf{k}_0 + \boldsymbol{\xi}) \\ &\quad + 2Q_z \mathcal{B}_1^{pq}(-\mathbf{k}_0, \mathbf{k}_0) \\ &= 2\left[\mathcal{B}_2^{pq}(-\mathbf{k}_0, \mathbf{k}_0; \mathbf{k}_0 + \boldsymbol{\xi}) + 2q_0 \mathcal{B}_1^{pq}(-\mathbf{k}_0, \mathbf{k}_0)\right]. \end{aligned} \tag{60}$$

To be consistent with the notation adopted in this paper, the elements of the SPM-1 and SPM-2 polarization matrices must be multiplied by $-2qq_0 = -2q_0^2$ in the backscattering direction.

Equation (60) behaves as $\mathbf{k}_0\cdot\boldsymbol{\xi}$ and $\boldsymbol{\xi}^2 = \xi^2$ evaluated at $\boldsymbol{\xi}' = \mathbf{k}_0 + \boldsymbol{\xi}$. Since in polar coordinates $\boldsymbol{\xi} = (\xi\cos\phi_\xi, \xi\sin\phi_\xi)$

$$\begin{cases} \boldsymbol{\xi}'^2 = k_0^2 + \xi^2 + 2k_0\xi\cos\left(\phi - \phi_\xi\right) \\ \mathbf{k}_0\cdot\boldsymbol{\xi}' = k_0^2 + k_0\xi\cos\left(\phi - \phi_\xi\right), \end{cases} \tag{61}$$

the elements $\{\mathcal{M}^{pq}(-\mathbf{k}_0, \mathbf{k}_0; \boldsymbol{\xi})\}$ are periodic functions with respect to the angle $\phi - \phi_\xi$. Moreover, one can notice that $\mathcal{M}^{VV}(-\mathbf{k}_0, \mathbf{k}_0; \mathbf{0}) = \mathcal{M}^{HH}(-\mathbf{k}_0, \mathbf{k}_0; \mathbf{0}) = 0$.

Appendix 4. Backscattering polarization matrices of the LCA2 kernel

In the backscattering direction, the elements of the KA-1 polarization matrix are [9,18]

$$\mathcal{K}_1^{VV,HH}(-\mathbf{k}_0,\mathbf{k}_0)=2K^2\mathcal{R}^{VV,HH}(q_0), \tag{62}$$

with

$$\begin{cases}\mathcal{R}^{VV}(q_0)=\frac{\epsilon_r q_0-\sqrt{(\epsilon_r-1)K^2+q_0^2}}{\epsilon_r q_0+\sqrt{(\epsilon_r-1)K^2+q_0^2}}\\ \mathcal{R}^{HH}(q_0)=\frac{q_0-\sqrt{(\epsilon_r-1)K^2+q_0^2}}{q_0+\sqrt{(\epsilon_r-1)K^2+q_0^2}}.\end{cases} \tag{63}$$

From Equation (58) multiplied by $-2q_0^2$ and from Equation (5), the elements $\mathcal{T}^{pq}(\mathbf{k},\mathbf{k}_0;\boldsymbol{\xi})=j\mathcal{N}_2^{pq}(\mathbf{k},\mathbf{k}_0;\boldsymbol{\xi})/Q_z$ are expressed in the backscattering direction as

$$\mathcal{T}^{pq}(\mathbf{k},\mathbf{k}_0;\boldsymbol{\xi})=\left[\mathcal{B}_1^{pq}(-\mathbf{k}_0,\mathbf{k}_0)-\mathcal{K}_1^{pq}(-\mathbf{k}_0,\mathbf{k}_0)\right]\big|_{\mathbf{k}_0=\boldsymbol{\xi}/2}. \tag{64}$$

Like the SSA-2 kernel $\mathcal{M}^{pq}$, $\mathcal{T}^{VV}(-\mathbf{k}_0,\mathbf{k}_0;\mathbf{0})=\mathcal{T}^{HH}(-\mathbf{k}_0,\mathbf{k}_0;\mathbf{0})=0$, and unlike the SSA-2 kernel, they are even functions with respect to ξ, because they depend only on $\boldsymbol{\xi}^2=\xi^2$. In addition, unlike the SSA-2 kernel, they are independent of $\mathbf{k}_0$. For a perfectly conducting surface ($\epsilon_r=i\infty$), one has

$$\mathcal{T}^{VV}\left(-\mathbf{k}_0,\mathbf{k}_0;\frac{\boldsymbol{\xi}}{2}\right)=\mathcal{T}^{HH}\left(-\mathbf{k}_0,\mathbf{k}_0;\frac{\boldsymbol{\xi}}{2}\right)=\frac{\xi^2}{2}. \tag{65}$$

In conclusion, the behaviour of the LCA-2 kernel with respect to $\boldsymbol{\xi}$ is very different from the SSA-2 one.

Appendix 5. Integrations over $\{\phi_r,\phi_\xi,\phi\}$ with $\hat{\mathcal{N}}_2^{pq}(\xi)\neq 0$

From Equations (24), (29), (30) and (32), the following triple integral must be derived

$$\int_0^{2\pi}\int_0^{2\pi}\int_0^{2\pi} e^{ja\cos(\phi-\phi_r)+jc\cos(\phi_\xi-\phi_r)-b\cos(2\phi_r)+s(\phi_\xi-v\phi)} \times\hat{W}_2(\xi,\phi_\xi)\cos(n\phi)\,d\phi_r d\phi_\xi d\phi, \tag{66}$$

where $a=k_{\mathrm{B}}r$, $b=Q_z^2W_2(r)$ and $c=\xi r$. In addition, the sea height spectrum is defined as $\hat{W}(\xi,\phi_\xi)=\frac{1}{2\pi}[\hat{W}_0(\xi)+\cos(2\phi_\xi)\hat{W}_2(\xi)]$.

5.1. *Term with respect to* $\hat{\boldsymbol{W}}_0(\boldsymbol{\xi})$

Using the same method as in Appendix 2, the integration over ϕ_r yields

$$\frac{1}{2\pi}\int_0^{2\pi} e^{ja\cos(\phi-\phi_r)+jc\cos(\phi_\xi-\phi_r)-b\cos(2\phi_r)+s(\phi_\xi-v\phi)}d\phi_r =\sum_{m,p}(-1)^pJ_{2m+p}(a)J_p(c)I_m(b)e^{j\phi(2m+p-sv)+j\phi_\xi(s-p)}. \tag{67}$$

Thus, the integration of Equation (67) over $\phi_\xi \in [0; 2\pi[$ leads to

$$\int_0^{2\pi} \text{Equation (67)} d\phi_\xi = 2\pi(-1)^s J_s(c) \sum_m J_{2m+s}(a) I_m(b) e^{j(2m+s-s\nu)\phi}$$
$$= 2\pi(-1)^s J_s(c) \sum_{m \text{ even}} J_{m+s}(a) I_{\frac{m}{2}}(b) e^{j(m+s-s\nu)\phi}. \tag{68}$$

The integration of Equation (68) multiplied by $e^{-jn\phi}$ over $\phi \in [0; 2\pi[$ gives

$$\int_0^{2\pi} \text{Equation (68)} e^{-jn\phi} d\phi = (2\pi)^2(-1)^s J_s(c) J_{n+s\nu}(a) I_{\frac{m_0}{2}}(b)$$
$$\text{with } m_0 = n - s + s\nu \text{ even}, \tag{69}$$

and

$$\text{Equation (66)} = 2\pi^2(-1)^s J_s(c) \hat{W}_0(\xi) \sum_{\gamma=\pm1} J_{n\gamma+s\nu}(a) I_{\frac{m_0}{2}}(b)$$
$$\text{with } m_0 = n\gamma - s + s\nu \text{ even}. \tag{70}$$

5.2. *Term with respect to $\hat{W}_2(\xi)$*

In this case, the integrand of Equation (67) must be multiplied by $\cos(2\phi_\xi) = \frac{1}{2}(e^{j2\phi_\xi} + e^{-j2\phi_\xi})$. Using the same method as previously, one has from (68) with $(s \to s + 2)$

$$\frac{1}{2\pi} \int_0^{2\pi} \int_0^{2\pi} e^{j2\phi_\xi} e^{ja\cos(\phi-\phi_r)+jc\cos(\phi_\xi-\phi_r)-b\cos(2\phi_r)+s(\phi_\xi-\nu\phi)} d\phi_r d\phi_\xi$$
$$= 2\pi(-1)^s J_{s+2}(c) \sum_{m \text{ even}} J_{m+s+2}(a) I_{\frac{m}{2}}(b) e^{j(m+s-s\nu+2)\phi}. \tag{71}$$

The integration of Equation (71) multiplied by $e^{-jn\phi}$ over $\phi \in [0; 2\pi[$ gives

$$\int_0^{2\pi} \text{Equation (71)} e^{-jn\phi} d\phi = (2\pi)^2(-1)^s J_{s+2}(c) J_{n+s\nu}(a) I_{\frac{m_0}{2}}(b)$$
$$\text{with } m_0 = n - s - 2 + s\nu \text{ even}. \tag{72}$$

Eventually,

$$\text{Equation (66)} = \pi^2(-1)^s \hat{W}_2(\xi) \sum_{\gamma_1=\pm1} \sum_{\gamma_2=\pm1} J_{s+2\gamma_2}(c) J_{n\gamma_1+s\nu}(a) I_{\frac{m_0}{2}}(b)$$
$$\text{with } m_0 = n\gamma_1 - s - 2\gamma_2 + s\nu \text{ even}. \tag{73}$$